Unveiling the potential of surfactant Pluronic-P123 application during the synthesis of Ni-hydrotalcite-derived catalysts for low-temperature CO2 methanation: A novel approach

Minh Nguyen-Quang, Federico Azzolina-Jury, Frédéric Thibault-Starzyk, Arnaud Travert, Magdalena Ziąbka, Bogdan Samojeden, Monika Motak, Patrick da Costa

Unveiling the potential of surfactant Pluronic-P123 application during the synthesis of Ni-hydrotalcite-derived catalysts for low-temperature CO_2 methanation: a novel approach

Minh Nguyen-Quang[a,b,c], Federico Azzolina-Jury[a,*], Frédéric Thibault-Starzyk[a], Arnaud Travert[a], Magdalena Ziąbka[b], Bogdan Samojeden[b], Monika Motak[b], Patrick Da Costa[c].

[a]Laboratoire Catalyse et Spectrochimie (LCS), CNRS-ENSICAEN-Université de Caen, 6 boulevard du Maréchal-Juin, 14000 Caen, France

[b]AGH University of Science and Technology, Al. Mickiewicza 30, 30-059 Kraków, Poland

[c]Institut Jean le Rond d'Alembert, Sorbonne Université, CNRS UMR 7190, 2 place de la gare de ceinture, 78210 Saint Cyr l'Ecole, France

Corresponding author: Federico Azzolina-Jury (federico.azzolina-jury@ensicaen.fr)

Graphical Abstract

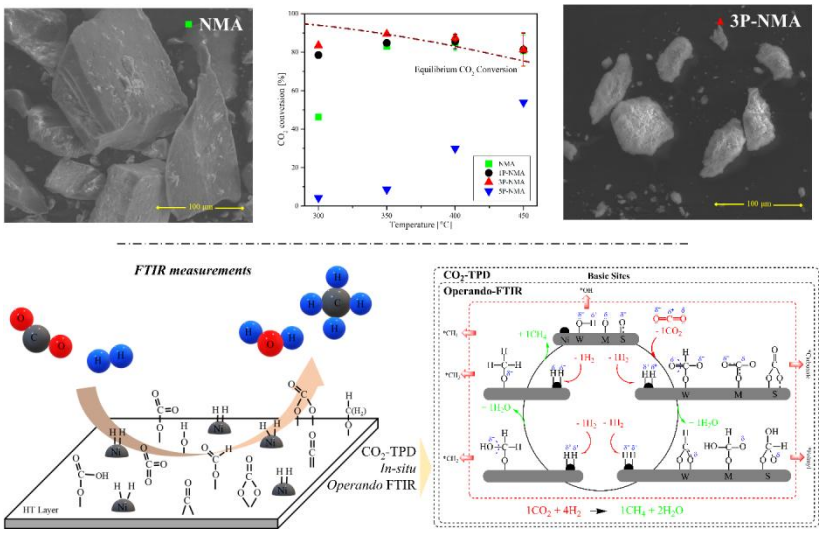

Abstract

For the tailoring purpose of NiMgAl-oxides (NMA) towards CO_2 methanation, the surfactant Pluronic-P123 was first-time employed at different concentrations. Catalysts were examined by SEM-EDX, BET, XRD, H_2-TPR, CO_2-TPD, and TGA. By adding P123, a clear revolution in terms of the texture, morphology, and pore of catalysts was observed, which has never been recorded previously. The correlations between carbonate species and basic sites were identified thanks to *in-situ* CO_2 sorption measurements. The stability of carbonate species was assumed to follow "hydrogen-carbonate < bidentate-carbonate < unidentate-carbonate < tridentate-carbonate". On the activity stand, 3P-NMA exhibited ca. 83.5% CO_2 conversion and 99.5% CH_4 selectivity at 300℃ vs. 46% and 97%, respectively, for the base case (GHSV = 12,000 h^{-1}, H_2/CO_2 = 4), alongside superior stability after a 16-hour of TOS run. Furthermore, *Operando* FTIR data revealed the appearance of formyl (*HCO) species under methanation conditions, allowing us to propose the reaction mechanism following *HCO formation as the key intermediate for CO_2 methanation.

Keywords: low-temperature CO_2 methanation, surfactant Pluronic P123, xP-NMA, HCO-intermediates, in-situ, Operando FTIR.

1. Introduction

Nowadays, severe environmental challenges such as global warming caused by the accumulation of the greenhouse gas CO_2 in the biosphere due to the world population expansion and massive energy consumption are becoming urgent. The CO_2 concentration in the air reached 418 ppm of threshold during December 2022 [1] and gestured a non-stoppable rise. It is thus indispensable to create breakthrough sustainable-green technologies to convert and ideally utilize CO_2 for long-term modern life evolution. Many efforts to lower CO_2 concentration in the biosphere have been engaged for directly capturing carbon dioxide from the atmosphere or the flue gas of fossil-fuel power plants and industrial processes [2, 3].

Carbon Capture and Storage processes (CCS) have been developed to capture and store CO_2 [3, 4]. CSS, however, can be hard to implement on an industrial scale for a number of reasons, including cost, transportation owing to the distance from locations, and the lack of knowledge in terms of long-term environmental safety [5]. One way to overcome this barrier would be CO_2 utilization, namely Carbon Capture and Utilization (CCU) [6, 7], a family of processes in which CO_2 extracted from human-induced processes can be converted into a variety of valuable-added products with the addition of a secondary substance and energy from renewable sources. Currently, carbon dioxide utilization following the CCU approach can be listed as a chemical feedstock or intermediate in just a few processes, including the manufacturing of urea, salicylic acid as a medicinal component, and polycarbonates.

CO_2 conversion into fuels such as methane or methanol has recently drawn much attention [8]. The Sabatier reaction [9] (Eq. 1), also known as the methanation of CO_2, is a promising strategy for converting CO_2 into useful substances [10, 11]. The National Aeronautics and Space Administration (NASA) has launched a significant effort in CO_2 methanation applications in spaceflight habitation on Mars, in which earth hydrogen is sent to Mars, allowing carbon dioxide in the Martian atmosphere to be converted into CH_4 and H_2O for energy and astronaut-life infrastructures, respectively [12].

CO_2 methanation is the reaction in which carbon dioxide and hydrogen are used as reactants in the catalytic generation of methane and water at temperatures ranging from 250°C to 550°C and pressure between 1 and 100 bar [13]. The reaction is thermodynamically favorable, with a negative Gibbs free energy (ΔG_{298K} = -130.8 kJ/mol); nevertheless, it is highly exothermic; thus, a complete reduction of carbon dioxide to methane is favored by low temperature and high pressure. Under mild reaction conditions, the equilibrium shifts towards the product side, according to Le Chatelier's principle [13, 14].

$$C^{+4}O_2 + 4H_2 \rightarrow C^{-4}H_4 + 2H_2O, \Delta H_{298K} = -165\ \mathrm{kJ/mol} \quad (\mathrm{Eq.}\,1)$$

Because the methanation reaction is an eight-electron process (the carbon oxidation number changing from +4 in CO_2 to -4 in CH_4) with considerable kinetic limitations, the requirement of a catalyst is mandatory. The most challenging task is developing a thermally stable catalyst with good activity and selectivity towards methane at moderate temperatures and pressures [15]. Various metals, principally based on Fe, Co, Ni, Rh, Ru, and Pt, among others, have been investigated as methanation catalysts, with Rh, Ru, and Ni being the most active for CO_2 methanation [16-20]. Nickel is particularly appealing for several reasons, including the fact that it is significantly less expensive than ruthenium [16] and rhodium [21], even though both are highly active and still being investigated. Furthermore, the availability of Ni in comparison to Ru and Rh is an essential factor in the industrial applications of Ni-based catalysts.

Aside from active metals, support substantially impacts the activity and stability of a catalyst [22-24]. Aluminum oxide, for example, is well-known for its large specific surface area (200-380 m^2/g_{cat}) [16, 25], whereas magnesium oxide, despite its moderate surface area, exhibits Lewis basicity - a property that enhances CO_2 adsorption capacity [26] and promotes coking resistance [27]. Designing Ni-based CO_2 methanation catalysts with improved low-temperature activity is, thereby, a continuing endeavor. Studies have been carried out with different supports and promoters, aiming to assist support-metal interactions, enhance the number and type of acidic and basic sites, tailor the particle size and dispersion to avoid sintering of Ni on the support [28-31] or understand and mitigate the deactivation [32]. Some could be listed, such as zeolites [31], La_2O_3 [33], CeO_2, Al_2O_3, TiO_2, MgO [34, 35], ZrO_2 [36], MOF [37], CNT [38], ...

Hydrotalcite-derived catalysts containing transition metals have lately stimulated the interest of researchers due to their (1) CO_2 adsorption capacity; (2) brucite layer cation-exchange ability; (3) interlayer space anion-exchange ability; and (4) adjustable surface basicity [39]. After calcination, hydrotalcite is converted into mixed oxides, which possess basic properties that facilitate CO_2 transformation [30, 40]. Upon H_2-reduction, active components with extensively dispersed metallic particles are frequently formed [40-43]. Furthermore, the versatility, simplicity, and low cost of this material are key advantages of its application [44].

Hydrotalcite-like compounds (HLCs) are characterized by the general formula (Eq. 2) [45]:

$$[M^{2+}_{1-x}M^{3+}_{x}(OH)_2]^{x+}[(A^{n-}_{x/n})^{x-}.mH_2O] \quad (\mathrm{Eq.}\,2)$$

Where M^{2+} and M^{3+} are different divalent and trivalent metal ions with $[M^{2+}_{1-x}M^{3+}_{x}(OH)_2]^{x+}$ representing the layer, and $[(A^{n-}_{x/n})^{x-}.mH_2O]$ indicating the interlayer composition. The interlayer anion, A, and the $M^{3+}/(M^{2+}+M^{3+})$ ratio, x, can vary between 0.20 and 0.40 [46, 47]. Only for the values of x between 0.2-0.33 crystalline hydrotalcite-like compounds can be obtained, with the value of x in natural compounds is generally 0.25. The kind of anion species that can be incorporated into the LDH structure has no practical limitations, that could be either mono- or di-valent anions; however, to synthesize

pure or well-crystalline materials, it is a challenge to avoid contamination by CO_2 in the aqueous solution when synthesizing hydrotalcite-like compounds (HTlcs) with anions other than carbonate, for example. Moreover, incorporating interlayer anions into the HTlc is also a significant aspect. Shigeo Miyata et al. [48] have established the affinity of interlayer anions as follows: $CO_3^{2-}>>SO_4^{2-}>>OH^->F^->Cl^->Br^->NO_3^->I^-$. Concerning synthesis routes, coprecipitation-based strategies at constant pH have been discovered to be the most often employed approach to this problem; where a solution comprising divalent and trivalent cation precursors is introduced to an alkaline mixture containing the anion, which will be intercalated in a certain-pH alkaline medium.

So far, to control such characteristic features of the Ni-HT, synthetic approaches have mainly dealt with incorporating a second metal, leading to bi-metallic catalysts [49-52]. Promoters, such as Cu [53], Y [54], La [55], Fe [56], Ru [57], and V [58], have been demonstrated as highly effective Ni-based catalysts towards CO_2 methanation. However, in addition to the support materials' chemical bulk characteristics, modifying the morphology and metals-HT framework interaction are critical factors but less studied. In this regard, our work has been dedicated to changing the properties of HT materials in terms of the surface, basicity, and stability in one-step synthesis.

On the other hand, in many contexts, SBA-15-supported catalysts exhibit several superior characteristics that aid chemical conversion, particularly a large surface area, highly uniform and orderly pore, and a very high stability due to the peculiarity of structural template Pluronic P123 [59]. However, in the present case, because of the basicity requirement for CO_2 methanation, the acidic-surface hydroxyl groups limit the application of such support for this reaction [60]. Still, the preparation method of SBA-15 - a hydrothermal synthesis with the triblock copolymer Pluronic P123 as a templating agent can be a source of inspiration for developing mesoporous-basic supports.

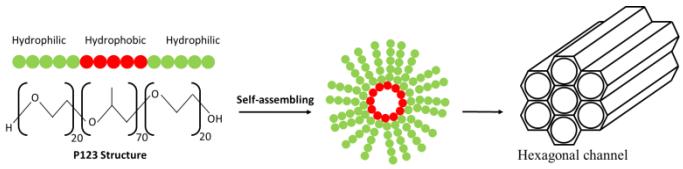

Figure 1. P123 structure and self-assembling mechanism of P123 in water

The Pluronic structure (P123) includes hydrophilic and hydrophobic heads, which will self-assemble to generate channels in the material. After thermal treatment, the structural template was removed, leaving porosity in the catalyst. Figure 1 depicts the self-assembling mechanism of P123 in water.

Following this line and for the first time, the present study used the Pluronic P123 to alter NiMgAl-hydrotalcite-derived catalysts. The structural template allows the basic properties of hydrotalcite material to be preserved while the surface area, the stability, on the other hand, may most undoubtedly be enhanced. NiMgAl-mixed-oxide derived from CO_3^{2-} hydrotalcite with x = 0.25 was initially synthesized as the parent catalyst, using the pH-constant technique in implementation. P123 was added in 1wt.%, 3wt.%, and 5wt.% as a modifying agent. All catalysts were tested under CO_2 methanation from 250 to 450°C.

2. Experimental

2.1. Development of the novel synthesis

In order to synthesize mixed-oxides derived from hydrotalcite catalysts, the co-precipitation method was followed, in which an aqueous solution of metallic cations (solution A) was introduced dropwise into a basic carbonate solution (solution B) at 65°C with stirring, as described elsewhere [61, 62]. To obtain solution A, nickel acetate salts ($Ni(Ac)_2.6H_2O$) (Avantor, Poland) and nitrate salts of magnesium and aluminum ($Mg(N)_2.6H_2O$, (Chempur, Poland), $Al(N)_3.9H_2O$), (Avantor, Poland) were soaked in distilled water at a molar ratio of $x = M^{3+}/(M^{2+} + M^{3+})$ of 0.25. Solution B was prepared by dissolving a proper quantity of Na_2CO_3 (Chempur, Poland) in water to achieve a $[CO_3^{2-}]$ of 1.0M. As the modification agent, a determined amount of surfactant Pluronic (P123) (Merck) was initially dissolved in solution B at 1wt.%, 3wt.%, and 5wt.%. In this study, the pH controller was NaOH 1M, which kept the pH of the mixture in the 9.5-10 range throughout the synthesis process.

As described earlier [61, 62], solution A was dropped into solution B in a beaker while vigorously stirring, keeping the temperature constant at 65°C. Following the co-precipitation step, the residual slurry was aged for 1 hour under the same conditions, keeping the pH unchanged. The obtained solid from vacuum filtering and washing with deionized water (65-80°C) till pH = 7, was then dried overnight at 80°C and followed the thermal treatment at 550°C for 5 hours with a 5°C/min heating ramp. After the calcination step, the catalysts containing NiMgAl were transformed into mixed-oxides form and denoted as NMA, 1P-NMA, 3P-NMA, and 5P-NMA.

2.2. Characterizations of the catalysts

2.2.1. Physicochemical characterizations

All catalysts were characterized via XRD, SEM-TEM, BET, H_2-TPR and CO_2-TPD, and TG techniques. Detailed information can be found in Supplementary notes.

2.2.2. IR characterization of CO_2 Sorption (in-situ measurements)

In-situ CO_2 adsorption and desorption experiments under static conditions at working temperature (250°C-450°C, 50°C/step) were carried out to first identify the possible surface species correlated to basic sites from CO_2-TPD measurements. Secondly, provide a clearer view of the stability of species formed on the catalyst surface. Spectra were collected by a Nicolet iS-5 spectrophotometer with a mercury-cadmium-telluride (MCT) detector, in the 4000-400 cm^{-1} range, at a resolution of 2 cm^{-1} and using 64 scans. The self-supporting wafer (ca. 20 mg, 18 mm in diameter) was initially activated at 450^0 C under flowing H_2/Ar (5% vol./vol.), then evacuated in Ar. The system is equipped with an automatic mechanism PELICAEN (the scheme and device can be found in Supplementary Figure 1), that automatically lifts and lowers the catalyst position to the IR-

beam zone. The CO_2 sorption protocol can be described as follows: first, the catalyst wafer was exposed to a pure CO_2 gas at static conditions, 10 torr, from room temperature to working temperatures (remained 10 min at each temperature) for adsorption experiments. After finishing the adsorption experiment at 450°C, the system was vacuuming flushed in order to remove weakly adsorbed species, and the temperature was lowered to 250°C before the desorption experiments. Spectra were collected after 10 min at each temperature for adsorption and desorption experiments. Before each measurement, the background was collected and used to subtract the absorbance from the other spectra.

2.3. Catalytic evaluation in CO_2 methanation as a function of temperature and Time On Stream (TOS run)

The catalytic activity was examined in a fixed-bed U-shaped reactor with a K-type thermocouple at temperatures ranging from 250°C to 450°C. Two layers of quartz wool were installed to cover the catalyst.

Before the reaction, the catalyst was reduced *in-situ* at 900℃ for 1 hour at a flow rate of 100 ml/min with a mixture of H_2 and Ar (5% vol./vol.). After the temperature had been decreased to 150℃, the gas was switched to the reactant flow, with $H_2/CO_2/Ar$ = 12/3/5 in a total flow rate of 100 ml/min controlled by 3 mass flow controllers (H_2/CO_2 = 4). Catalytic performances were measured from 250°C to 450°C in steps of 50°C, with the steady-state kept for 30 minutes at each temperature and a ramp at 10°C/min between each step. In our investigations, the mass of the catalyst was calculated based on its own density in order to achieve 12,000 h^{-1} of gas hourly space velocity (GHSV).

A gas chromatograph (490Varian Micro-GC) with a thermal conductivity detector was used to analyze the outlet. The catalytic activity was evaluated via CO_2 conversion and CH_4 selectivity, which were defined as follows (Eq. 3 and 4):

$$X_{CO_2}(\%) = \frac{[CO_2]^{in} - [CO_2]^{out}}{[CO_2]^{in}} = \frac{nCO_2{}^{in}.F^{in} - nCO_2{}^{out}.F^{out}}{nCO_2{}^{in}.F^{in}} \quad (Eq.\,3)$$

$$S_{CH4}(\%) = \frac{[CH_4]^{out}}{[CO_2]^{in} - [CO_2]^{out}} = \frac{nCH_4{}^{out}.F^{out}}{nCH_4{}^{out}.F^{out} + nCO^{out}.F^{out}} \quad (Eq.\,4)$$

where in- and out- terms correspond to the input and the output, and n- is the molar concentration of CO_2, CH_4, and CO measured by GC, respectively. F is represented to the total flow rate. Assuming that CH_4 and CO are the main-, and by-products of CO_2 methanation, Eq. 4 could be used to calculate the CH_4 selectivity.

Site-Time-Yield [63] of CH_4 (Eq. 5) was monitored, with n_{CH4} being the flow of CH_4 in the outlet [mmol.h^{-1}] and m_{cat} is the sample weight (g_{cat}) [64], respectively.

$$STY_{CH4}, (mmol./g_{cat}.h) = \frac{n_{CH4}}{m_{cat}} \quad (Eq.\,5)$$

The definition of the Site-time-yield can be stated as the rate of the catalytic reaction over the total number of accessible sites present in the reactor.

The stability of catalysts was examined by keeping track of the conversion and selectivity evolution by time-on-stream run over a considerable period of 16 hours at 300°C.

2.4. *Operando* FTIR Experiments

To get a deeper insight into the behavior of the parent catalyst (NMA) and catalyst modified by P123 (3P-NMA), *Operando* FT-IR CO_2 adsorption and methanation measurements were carried out at 300°C.

The *Operando* setup includes connections, and the analysis methodology was previously described in [65] (the system layout are presented in Supplementary Figure 2), where the measurements were performed in transmission mode with a Nicolet 6700 FT-IR spectrometer coupled with an MCT detector). FTIR spectra with a resolution of 4 cm^{-1} were acquired using 64 scans of each spectrum. The catalysts were positioned in the reactor cell between two KBr windows in self-supporting wafers of 20 mg (the same as *in-situ* CO_2 sorption measurements). In this scenario, the system setup allows for distinct diagnostics of gas-phase and surface evolutions by switching between two-mode measurements.

Following the same reduction procedure as the reaction, catalysts were reduced at 900°C. In order to remove contaminates and weakly pre-adsorbed species surely, the wafer was reduced again at 450°C for 1 hour in the flow of H_2/Ar, 10 ml/min (5% vol./vol.), and Ar purged the system prior to measurements.

CO_2 adsorption: CO_2/Ar (10% vol./vol.) total flowrate of 10 ml/min, CO_2 adsorption was kept for 30 min at 300°C. After that, the flow was switched to 10 ml/min of Ar to flush the weakly adsorbed species on the catalyst surface before methanation.

CO_2 methanation: $H_2/CO_2/Ar$ = 4/1/5 ml/min at a total flowrate of 10 ml/min; methanation was carried out for 30 min at 300°C.

In both cases of *in-situ* and *Operando* experiments, spectra were collected and treated using OMNIC® software.

2.5. Spent catalyst evaluations

In order to evaluate the catalysts after the reaction, wide Angle X-ray Diffraction, Thermogravimetric analysis, and Scanning electron microscopy-energy dispersive X-ray spectrometry were carried out. The configurations and program for measuring can be revised in Supplementary notes.

3. Results and discussion

3.1. Structural properties of NMA catalysts

3.1.1. Textural properties and morphology of catalysts

Micrographs of the P123-NMA series and element mapping on NMA and 3P-NMA are shown in Figure 2. As can be observed, all catalysts were formed as nanoparticle aggregates [66]. The parent NMA generally formed particles with irregular grains (Figure 2, top-left), which agreed with observed results in earlier studies [45, 67, 68]. The particles of mixed oxides with incorporated P123 had a more irregular appearance, with smaller particle sizes. Amazingly, while NMA displayed a solid structure, all catalysts prepared

with P123 demonstrated soft, porous/spongy-like structures. The element mapping, furthermore, indicated a homogeneous distribution of Ni (green), Mg (blue), and Al (red) on the entire NMA and 3P-NMA catalysts after reduction.

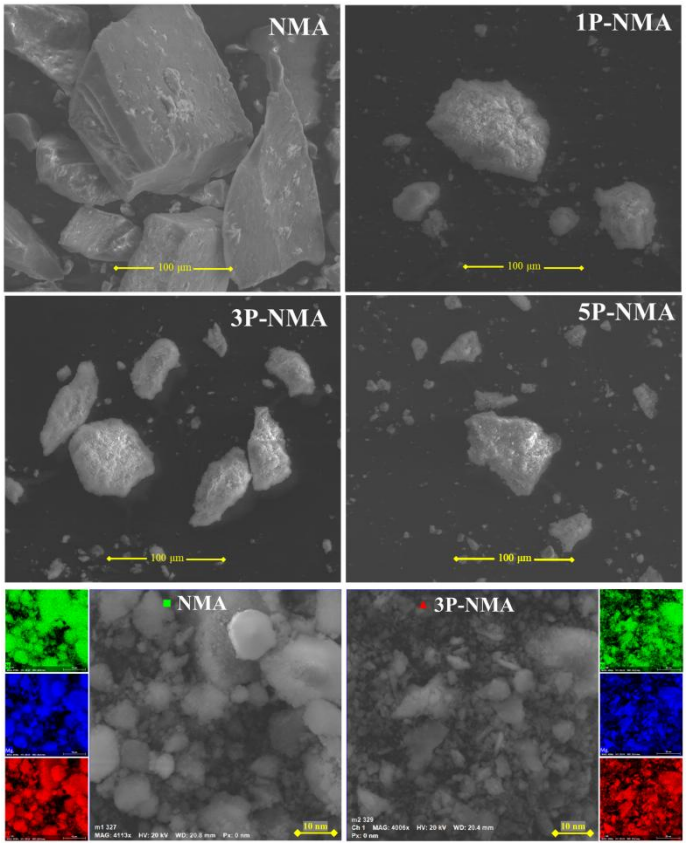

Figure 2. SEM images of calcined and reduced catalysts.

Additionally, EDX analysis (Supplementary Table 1) revealed an increase in oxygen content concurrent with a decrease in Ni concentration in all catalysts prepared with P123. These observations visually suggested a total change in the morphology of materials modified by P123 that has never been reported before in the literature.

Additionally, in order to clarify the critical influences of P123 on catalyst structure, TEM measurements were carried out for the reduced NMA and 3P-NMA catalysts. The catalysts were reduced under the same conditions as the reaction, TEM on the reduced catalysts, therefore, can offer information on the active form of the catalysts. Figure 3. depicts the acquired results, with (a), (b) present NMA and (c), (d) on 3P-NMA.

When (a) and (c) were compared, it was obvious that 3P-NMA had substantially smaller Ni^0 particle sizes. Metallic Ni^0 seemed to be aggregated in the NMA sample rather than well distributed on 3P-NMA, which resulted in the formation of clusters in the NMA catalyst.

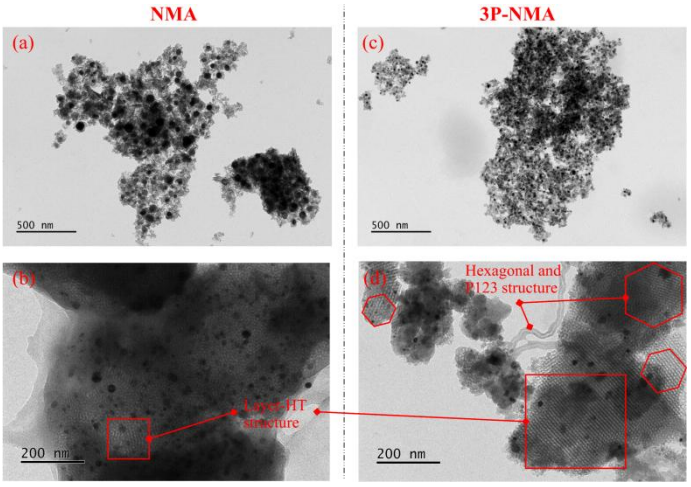

Figure 3. TEM images of reduced NMA (a, b) and 3P-NMA (c, d).

On the other hand, (b) exhibited the layered structure on NMA found in small region of captured zone, demonstrating that it was properly synthesized. On the other hand, the layer structure of 3P-NMA (d) indicated the well-ordered arrangement across the entire captured zone. Interestingly, the hexagonal channel of structural template P123 was discovered on 3P-NMA (d). We deduced this phenomenon occurred as a result of the self-assembling mechanism of P123, as proposed in Figure 1. In the initial solution, P123 was self-assembled, generating the foundation of the spatial template; metallic cations following the co-precipitation were formed on this architecture. Consequently, the structural layers were reconstructed contemporaneously with the establishment of hexagonal channels. After the thermal treatment steps, P123 was removed, leaving the catalysts with an ordered and homogenous structure. In this sense, P123 successfully modified the catalyst structure.

3.1.2. BET surface area and pore size distribution

The N_2 adsorption-desorption for all calcined catalysts is presented in Figure 4a. According to IUPAC categorization, all hydrotalcite-derived materials have type IV-N_2 sorption isotherms, which was in accordance with the literature [62, 69, 70].

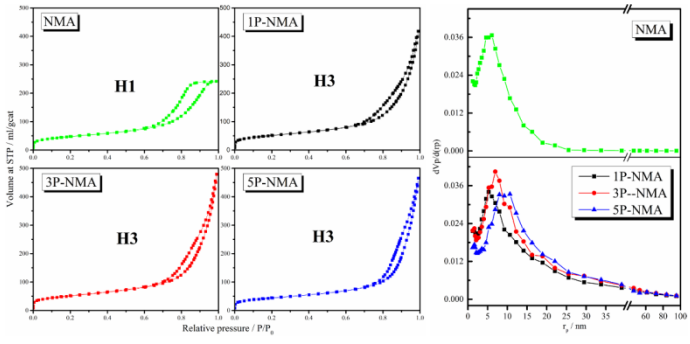

(a) (b)

Figure 4. (a) N_2 adsorption-desorption and (b) pore size distributions of all calcined catalysts.

Interestingly, the changes in the P123-modified catalyst isotherms were clearly seen. More specifically, these isotherms exhibited an H3-hysteresis loop at a higher volume at STP (ml/g_{cat}) than the parent NMA, which displayed an H1-type hysteresis loop. This latter result, together with the changes in morphological structure revealed by SEM and TEM, confirmed that surfactant P123 completely changed the textural properties of the hydrotalcite materials. As discussed, the reorientation of HT layering by P123 was the reason why all catalysts containing P123 became more layered compared to the parent NMA.

The measured mean pore diameter (Table 1) clearly showed a pore enlargement after modification by P123. As its value for NMA was about 4.6 nm, while for 1P-NMA, 3P-NMA, and 5P-NMA, the values were ca. 5.1 nm, 8.0 nm, and 10.7 nm, respectively. The specific surface area (SSA, calculated from the BET method) and pore volume (from the BJH method) are summarized in Table 1. In terms of texture and morphology, the preliminary effects of employing P123 during NMA synthesis were obvious. P123 not only rearranged the catalyst layers but also generated the hexagonal channel and expanded the pore without affecting the inherent hydrotalcite properties.

Table 1. Physicochemical properties of calcined sample: BET surface area, total pore volume, and pore sizes.

Catalysts	S_{BET} (m^2/g)[a]	Pore volume (cm^3/g)[b]	r_p, (nm)[c]
NMA	165	0.36	4.6
1P-NMA	177	0.62	5.1
3P-NMA	178	0.73	8.0
5P-NMA	152	0.97	10.7

[a]Specific surface area from BET method.

[b]Pore volume determined from the adsorption isotherms by the BJH method.

[c]Mean pore diameter (r_p).

Table 1 showed that the surface area increased from 165 m^2/g (NMA) to 177 m^2/g and 178 m^2/g, respectively, once 1wt% and 3wt% P123 was introduced. It is worth noticing that the surface areas of 1P-NMA and 3P-NMA were identical, even though adding 5wt% P123 lowered the total surface area to 152 m^2/g. Since this surface area was smaller (8% less) than that of parent NMA, it is reasonable to assume that adding 3wt% was the maximum amount that could drastically improve HT surface area. A larger quantity might likely overstretch the pores, causing displacement of the HT structure. Additionally, adding 5 %wt. P123 caused the increase in the surface NiO particle size from 2.55 nm (NMA) to 4.49 nm of 5P-NMA, which was nearly double the value (this will be addressed in the next section *3.1.3. Crystallinity state of catalysts*). These factors together logically contributed to the partial blocking of the smaller pore, resulting in a loss in SSA. The surface area in the 5P-NMA catalyst was possibly contributed by the larger pores. It explained why 5P-NMA had a larger pore size (consequently, a higher pore volume) yet a lower SSA.

3.1.3. Crystallinity state of catalysts

Figure 5 shows the diffractograms of calcined at 550°C and non-calcined samples. There were some noticeable changes in XRD profiles between calcined and dried samples; however, distinctive peaks indicating the presence of structures, that had previously been documented for hydrotalcite materials [47], were confirmed.

For dried samples (represented by the dashed lines), the basal (003), (006), and (009) planes reflected narrow, symmetric, and intense reflections at lower 2θ angle regions, while the non-basal (015), (018) (JCPDF file 00-15-0087) planes had broader, more minor reflections at higher angles [66, 71, 72]. These diffraction patterns indicated the good crystallinity of the prepared catalysts.

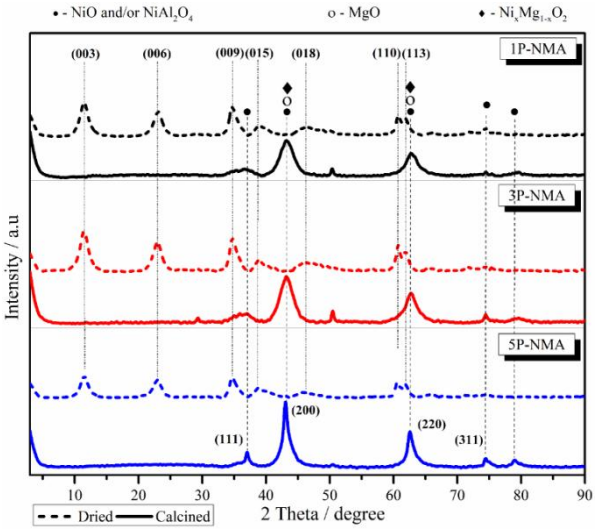

Figure 5. WAXD results of dried (dashed lines) and calcined (continuous lines) catalysts.

Upon calcination (continuous lines), the reflections of NiO were the only ones visible, suggesting well-dispersed Mg,Al-species in the oxide matrix. The removal of the (003), (006), and (009) planes revealed the disorder in the stacking of the catalyst layers following the thermal treatment. Reflections arising at 2θ angle = 37.3^0 , 43.2^0 , 62.8^0 , and 75.6^0 , respectively, can be identified as (111), (200), (220), and (311) crystal planes of the bulk NiO, suggesting the presence of NiO, $NiAl_2O_4$, MgO, and NiO/MgO defined as $Ni_xMg_{(1-x)}O_2$ [71-73] in the framework. According to the standard spectrum, these diffraction peaks (positions and relative intensities) were characteristic of NiO Face-Centered Cubic crystalline structure (JCPDS, No. 04-0835). No additional phase was found, implying that Mg^{2+} cations had been isomorphically substituted by Ni^{2+} and Al^{3+} in the brucite-like layers [70].

Impact of the preparation on the bulk parameters of the hydrotalcite-based catalysts was evaluated via lattice parameters *a* and *c* (Supplementary Eq. 2), and the values are reported in Table 2.

Table 2. Structural parameters calculated from XRD measurements

Catalysts	Structural parameters		
	NiO Particle size (nm)	a* (Å)	c** (Å)
NMA	2.55	3.05	23.33
1P-NMA	2.45	3.05	23.14
3P-NMA	2.56	3.05	23.22
5P-NMA	4.49	3.05	23.16

*Calculated from d-spacing of (110) plane; $a = 2.d_{(110)}$

**Calculated from appropriate d-spacings of (003), (006) and (009) planes: $c = d_{(003)} + 2.d_{(006)} + 3.d_{(009)}$

The *a* parameter was identical for all materials at 3.05 Å and close to the theoretical values for brucite layers [74], implying the absence of lattice distortions. Furthermore, in contrast to the NMA material, the obtained *c* values, which corresponded to the triple thickness between brucite layers in hydrotalcite structure, somewhat decreased for samples prepared with P123. These values indicated the modification of NMA by P123. All calcined catalysts had a related-metallic NiO phase with particle sizes ranging from 2.5 nm in NMA to 4.5 nm in 5P-NMA, suggesting that the Ni particle size in the modified materials was proportional to the P123 content. It is worth noting that smaller nickel particles correlate with higher metal dispersion, and the smaller nickel particles assist in hydrogenating carbon dioxide to methane. Consequently, 1P123 and 3P-NMA could be expected to deliver high catalytic performance.

3.1.4. On the reducibility of Ni-species

The H_2-TPR was investigated to understand better the reducibility of Ni in the xP-NMA catalyst series. Multiple peaks could be seen in the TPR profiles in the temperature range of 100-900°C. Peaks at approximately 200°C, 300°C, 400°C, 500°C, 620°C, as well as a massive reduction peak around 700-800°C could be identified, which corresponded to Ni-species in various phases of interaction with hydrotalcite-derived materials. These reduction peaks might be separated into two groups: one for lower reduction temperatures (100-550°C) and another for higher reduction temperatures (600-800°C).

A deeper look at the temperature range of 100-550°C indicated that the rapid reduction of NiO species was linked to the first two peaks that emerged at around 185°C-205°C and ca. 294°C. These low-temperature peaks accounted for most reductions of the isolated NiO [75] and NiO non-uniformly dispersed on the support surface. When compared to NMA, only the first peak at ca. 200°C was visible, indicating that more easily reduced NiO species had been produced by adding P123. Nevertheless, the reduction peaks of 5P-NMA were hardly seen in this temperature range. The more intense peaks that appeared at a maximum temperature of around 396°C and 506°C were due to a reduction in free-bulk NiO/well-dispersed NiO and bulk NiO weakly interacting with the Mg(Al)O phase [76], respectively.

The addition of P123 enabled this interaction to be altered, resulting in lower reduction temperatures (maxima at ca. 380°C and 485°C for 1P-NMA 3P-NMA vs. 396°C and 506°C for NMA). This is also linked to a dilution of Ni when P123 was added, as evidenced by the EDX data in Supplementary Table 1, in which it has been reported in the literature [77] and was thought to be caused by an increase in foreign ions (Mg^{2+} and/or primarily Al^{3+}) within the NiO phase. A high-intensity reduction peak at 379°C together with a broad base at a high-temperature range for the 3P-NMA profile demonstrated that the NiO species of this catalyst was easily reduced and uniformly distributed. The corresponding reduction peak of 5P-NMA shifted towards higher temperatures with decreasing intensities and became wider, indicating that the proper P123 concentration was favorable to the generation of small and uniformly distributed-Ni particles (c.f. Table 2). As a result, the catalytic activity of CO_2 methanation can be significantly influenced. Overall, Eq. 7 could be used to illustrate such reduction in the 250-550°C range:

$$NiO + H_2 = Ni^0 + H_2O \text{ (Eq. 7)}$$

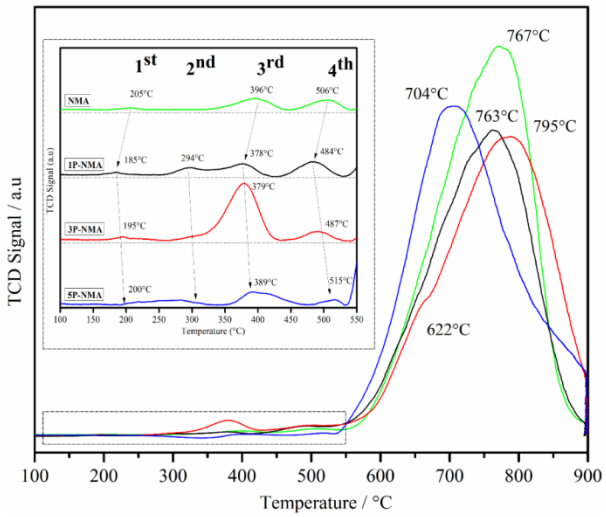

Figure 6. H_2-TPR profiles of xP-NMA series

At a higher reduction temperature, the shoulder peak of about 622°C was attributed to the reduction of non-stoichiometric amorphous nickel aluminate [78] (Eq. 8):

$$Ni_xAl_2O_{3+x} + xH_2 = xNi^0 + xH_2O + Al_2O_3 \text{ (Eq. 8)}$$

Finally, the reduction of stoichiometric $NiAl_2O_4$ species was registered as the highest hydrogen consumption for the most prominent peak observed on the isothermal stage at 700-800°C [27, 79]:

$$NiAl_2O_4 + H_2 = Ni^0 + H_2O + Al_2O_3 \text{ (Eq. 9)}$$

Compared to NMA, such band position did not change much for 1P-NMA (763°C vs. 767°C), slightly shifted toward a higher temperature for 3P-NMA (795°C) and shifted backward to a much lower temperature for 5P-NMA (704°C). This showed that adding 3 wt.% P123 to the catalyst potentially enhanced the interaction between NiO and the metal oxide support, while this was not the case with the 5P-NMA catalyst, as seen by the position of the reduction peak, which consumed 99.6% of the hydrogen (Table 3).

Table 3. H_2 consumption calculation and distribution of reduction peaks

Catalysts	Total H_2 consumption ($mmol/g_{cat}$)	% Peak consumption			
		1st peak	2nd peak	3rd peak	4th peak
NMA	4.34	0.07	0.07	63.15	36.71
1P-NMA	3.53	0.70	0.30	61.04	37.96
3P-NMA	3.62	1.32	0.20	63.34	35.14
5P-NMA	4.11	0.36	0.01	99.63	

The results from Table 3 suggested that while adding 5 wt.% P123 has a substantial impact on reduction profiles, it had a minor influence on overall H_2 consumption, which ranged from 3.53 to 4.34 $mmol/g_{cat}$ for all catalysts. Herein, we believed that the use of P123 during catalyst synthesis enabled Ni^{2+}, Mg^{2+}, and Al^{3+} to be co-precipitated in

different manners, resulting in the modification of the Ni-matrix interactions. Importantly, adding 1 and 3 %wt. P123 enhanced the incorporation of Ni^{2+} into the framework while weakening the reducibility, which was evidenced by the shift of the reduction peaks to higher temperatures and the lower H_2 uptake, respectively. The overstretch by adding 5 %wt. P123 made the reconstruction of the catalyst to be inefficient. Furthermore, the interaction of cations found on 5P-NMA mainly to be $NiAl_2O_4$ spinel with 99.6% hydrogen consumption; it explained the bigger particle size found by XRD analysis.

3.1.5. Effect of P123 concentration on the basic properties of catalysts

CO_2-temperature programmed desorption had used to explore the basicity of the catalysts further. CO_2-TPD profiles of catalysts can be found in Supplementary Figure 3, in which three peaks denoting weak, medium, and strong sites were recognized at 120-150^0 C, 270-340^0 C, and around 550^0 C for all xP-NMA series. No CO_2 desorption peak was found above 600^0 C.

The first desorption peak was assigned to CO_2 desorption from the surface basic OH-group (hydrogen carbonate species), whereas the medium-strength basic sites were centered around 270-340^0 C, corresponding to CO_2 desorption from metal-oxygen pairs (Mg^{2+}-O^{2-}, Al^{3+}-O^{2-} pairs) which were known as carbonate species [80, 81]. Finally, CO_2 desorbed from strong-basic sites at higher temperatures, as observed for hydrotalcite-derived catalysts via the CO_2-bond on the low oxygen co-ordination anion [82-86].

In order to identify the carbonate species-related basicity, infrared spectroscopy examination of the surfaces of the mixed oxides upon CO_2 adsorption near room temperatures was executed to further describe the basic sites of the catalysts. Figure 7 shows the FTIR spectra of the previously selected mixed oxides (3P-NMA) after CO_2 adsorption at room temperature in the 1900-950 cm^{-1} range.

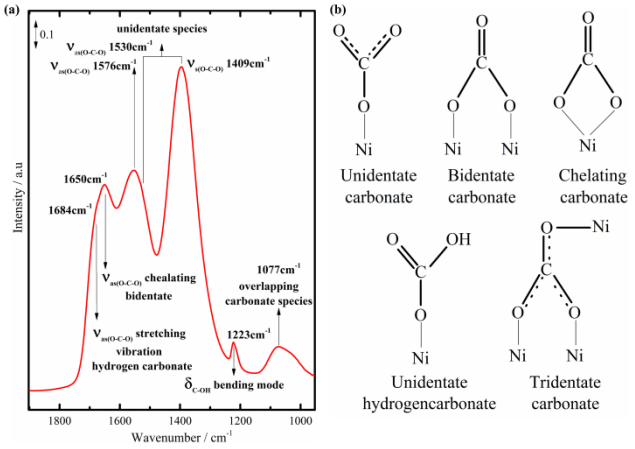

Figure 7. (a) Infrared spectra of CO_2 adsorbed on 3P-NMA after 30min and (b) Possible species appeared in the CO_2 adsorption experiment.

The assignments of the IR bands to the species formed on the 3P-NMA surface are shown in Figure 7a. Note that the CO_2 adsorption experiment was carried out near RT; thus, species observed by IR spectroscopy are the same as those adsorbed in CO_2-TPD measurement. The carbonate species formed on surface oxygen atoms with various degrees of coordination, resulting in unidentate, bidentate chelating, and bridging carbonate species. The structure of these species can be reviewed in Figure 7b.

In-situ CO_2 sorption measurements at static conditions under working temperatures (250-450°C): In order to interpret the formation and the thermal stability of carbonate species, the temperature dependence of these bands was investigated by undertaking CO_2 adsorption and desorption experiments at static temperatures of 250°C, 300°C, 350°C, 400°C, and 450°C.

The initial presence of carbonate species on the parent NMA catalyst after calcination at 550°C, after reduction at 900°C, and re-reduced at 450°C before the experiment was first determined. The results are plotted in Figure 8, where carbonate species (ranging from 1595 cm^{-1} to 950 cm^{-1}) were found at all conditions, with the most significant number belonging to calcined samples along the absorbed water (broad $\tau(H_2O)$ stretching band from 3000 cm^{-1} to 3800 cm^{-1}.

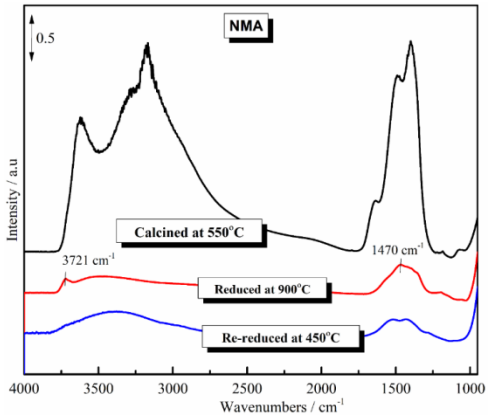

Figure 8. Infrared spectra of NMA after calcination, reduction at 900℃ and re-reduction at 450℃

After reducing at 900°C (red), absorbed water and carbonate species vastly decreased. The stretching vibration of OH from water in the interlayer space $\tau(H_2O)$, which was accountable for a band at 3721 $cm^{-1,}$ was observed. The band at 1470 cm^{-1} was associated with the hydrogen carbonate species [26, 87] and has vanished by re-reduction at 450°C (blue). In this sense, it is necessary to remove all adsorbed species before CO_2 sorption experiments. In the following experiments, therefore, all catalysts were re-reduced at 450℃ before conducting experiments. The CO_2 sorption results are reported in Figure 9, with corresponding adsorption behaviors (left) and desorption behaviors (right).

Regarding CO_2 adsorption results, in detail, CO_2 adsorption on the NMA at high temperatures resulted in CO forming, leading to bands around 1930 cm^{-1}, 2067 cm^{-1}, 2081 cm^{-1}, and 2283 cm^{-1} [88]. The IR band at 1930 cm^{-1} was attributed to the mono carbonyl formed on the Ni site (C=O stretching mode). The two later bands at 2067 cm^{-1} and 2086 cm^{-1} were due to the di-carbonyl on the surface [88-90].

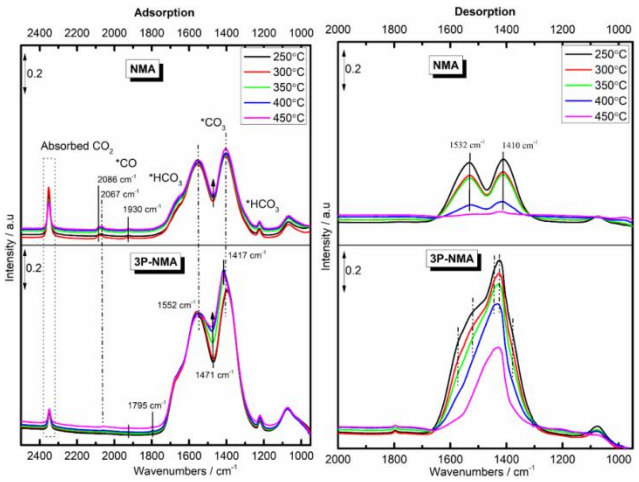

Figure 9. Collected spectra of the catalysts during the CO_2 adsorption (left) and CO_2 desorption (right) experiment at different temperatures. Spectra are recorded at room temperature.

Interestingly, in the case of 3P-NMA, those carbonyl band intensities were observed at a much lower intensity. In addition to the bands at 1552 cm^{-1} and 1410 cm^{-1} (which shifted from 1393 cm^{-1} when temperature up to 350°C-green, blue, and pink lines and with higher intensity than NMA), a novel IR band at ca. 1795 cm^{-1} could be observed. This IR band was ascribed to the polydentate bidentate (ν_{as} mode) species, according to [91], while the others belong to symmetric and antisymmetric (COO) vibration of unidentate carbonate, found at slightly different positions with respect to NMA catalyst. The total basicity could be the reason for this different behavior, as CO_2-TPD indicated that NMA modified by P123 led to a double amount of basicity. It was, therefore, suggested that preparing NMA with P123 seems to function for CO_2 to be directly absorbed on the catalyst surface, resulting in the formation of various carbonate species. While CO_2 tends to be firstly dissociated into CO and O_2, CO was then adsorbed into NMA surface to generate more carbonyl species.

In terms of desorption behavior - thermal stabilization (Figure 9, right), desorption at 250°C first resulted in the elimination of all carbonyl groups and all hydrogen carbonate species, whereas a proportion of unidentate carbonate remained. Precisely, the collapse of the unidentate species and the drop of the bands at 1685, 1646, and 1221 cm^{-1} [91] corresponding to unstable hydrogen carbonate species were seen for NMA at the starting temperature of 250°C. Unidentate carbonate (1410 cm^{-1} and 1530 cm^{-1}) [91] persisted at lower intensities with the increase in temperature, and the 1530 cm^{-1} band [91, 92] (asymmetric COO stretching) vanished at increasing temperatures up to 450°C.

The persistence of unidentate carbonate on 3P-NMA could be noted; nevertheless, the bicarbonate species corresponding to those bands at 1410 cm^{-1} and 1551 cm^{-1} (unidentate carbonate [91]) did not disappear at 450°C. Interestingly, the band around 1797 cm^{-1} [88] corresponding to polydentate species appeared to be stable for all conditions, with lower intensity at the higher temperature. The sum of measurements and correlation between the basic sites and the IR bands are presented for the first time in Table 4.

Table 4. Correlation between CO_2-TPD and *in-situ* CO_2 sorption experiments

Basic sites (CO_2-TPD)		*in-situ* CO_2 sorption	Thermal Stabilization
Weak (120-150^0 C)	OH-basic, free carbonate, physically adsorbed carbonate.	Hydrogen carbonate	< 250°C
Medium (270-340^0 C)	Forming on metal-oxygen pairs Mn^{2+}-O^{2-}, Al^{3+}-O^{2-}, requires the participation of surrounding cationic sites.	Bidentate carbonate (Chelating, Bridging)	250-450°C
Strong (550^0 C)	Arising on oxygen anions at the lowest coordination number (O^{2-}).	Unidentate carbonate	> 450°C
Hydrogen carbonate < Bidentate (chelating and bridging) carbonate < Unidentate species < Tridentate carbonate			
(This work)	[80-86]	[26, 87-91]	**This work**

Alongside the deactivation of Ni-catalyst and reverse water gas shift (RWGS) reaction occurring at high temperatures, the stabilization of those carbonate species could negatively contribute to the overall activity.

Following the TPD results, the desorption peaks of all P123-containing catalysts showed a shift toward higher temperatures but remained at lower temperatures than for NMA, implying the incorporation of P123 into NiMgAl assisted the formation of weaker basic sites. Furthermore, the CO_2-TPD profiles obtained for P123-modified solids could be divided into two groups with similar profiles: (1) NMA, 5P-NMA, and (2) 1P123 and 3P-NMA, the primary difference being greater CO_2 desorption from strong basic-sites.

In the literature, weak and medium basic sites were reported to lead to CO_2 adsorption and activation [30], actively contributing to CO_2 methanation. The CO_2 molecules would be adsorbed and dissociated on the support surface to form various carbonate species (*the formation, identification, and stabilization of carbonate species could be reviewed in the upper part*), then combined with the active H generated on the Ni-metallic site to produce the final product methane [30, 93]. Therefore, alongside validating carbonate species (basicity) on catalysts, the total amount of basic sites was calculated by integrating the CO_2-TPD peaks. Data are presented in Table 5.

Table 5. Calculated basicity for xP-NMA series

Catalysts	Total basicity (µmol/g_{cat})	% Basic sites		
		Weak	Medium	Strong
NMA	57	22.5	60.0	17.5
1P-NMA	115	11.9	52.8	35.3
3P-NMA	121	20.2	58.2	21.6
5P-NMA	79	29.8	58.5	11.7

Overall, all catalysts containing P123 exhibited a higher total number of basic sites than the parent NMA. Among the studied catalysts, the 1P123 and 3P123 revealed the highest total number of basic sites of ca. 115-121 µmole/g_{cat}. On the other hand, it was found to be substantially lower for the 5P-NMA catalyst, dropping to 79 µmole/g_{cat}. The fact that adding P123 into HT-material could lower the amount of strong-basic site and increase the weak-basic site at the same time while the medium-basic site witnessed

around 53-60%. It seems that changing P123 concentrations mainly affected weak and strong sites' distribution.

The total amount of weak and medium sites calculated can be placed in the order of NMA (47 µmol/g_{cat}) < 5P-NMA (69 µmol/g_{cat}) < 1P-NMA (74 µmol/g_{cat}) < 3P-NMA (95 µmole/g_{cat}).

3.2. Catalytic performance in CO_2 methanation

The CO_2 conversions (a), CH_4 selectivity (b) of the catalysts as a function of the reaction temperature alongside the TOS assessment and TOF values (c) are presented in Figure 10.

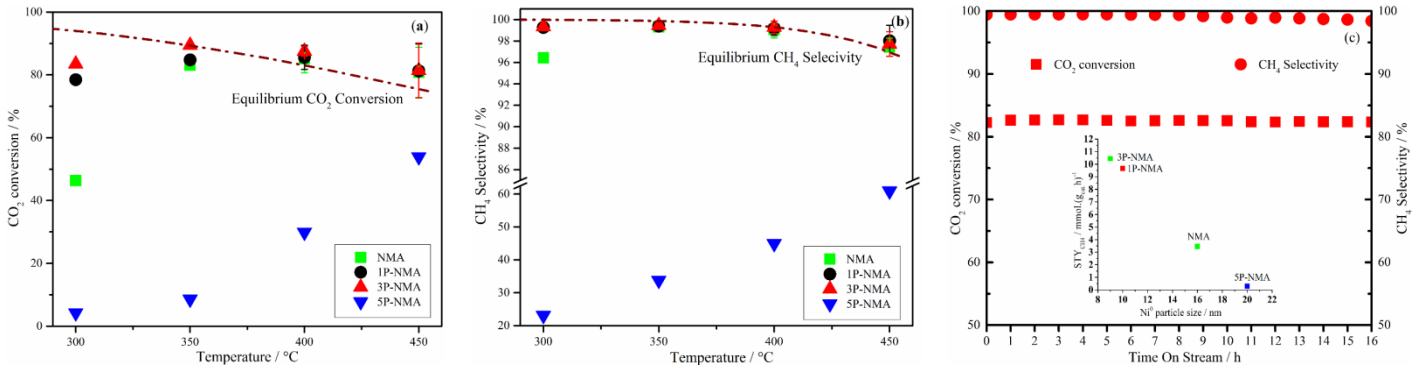

Figure 10. (a) CO_2 conversion and (b) CH_4 selectivity of all catalysts under CO_2 methanation tests, and (c) TOS run on 3P-NMA catalyst and STY_{CH4} calculation at 300°C (conditions: GHSV = 12,000 h^{-1}, F = 100 ml/min, $H_2/CO_2/Ar$ = 60/15/25). The dashed lines reflect the thermodynamic equilibrium of CO_2 conversion and CH_4 selectivity.

The CO_2 methanation was initiated at 250°C and reached 46% CO_2 conversion at 300°C for the non-modified HT-derived catalyst (NMA), with ca. 97% selectivity of CH_4. When the temperature increased to 350°C, the CO_2 conversion reached a maximum of 82% maximum, with 99.6% CH_4 selectivity. Both CO_2 conversion and CH_4 selectivity remained as high as 81% and above 97%, respectively, up to 450°C.

Catalysts containing 1 wt%. P123 exhibited better performance. As demonstrated by Figure 10a, CO_2 conversion reached 79% at 300℃. This value increased further and peaked at 400°C with a maximum conversion of 86% and 99.7% CH_4 selectivity.

In our study, the best performance was observed for the 3P-NMA catalyst with ca. 83.5% and nearly 90% CO_2 conversion at 300℃ and 350℃, respectively. Figure 10b also showed a remarkable CH_4 selectivity for this catalyst at medium temperature (ca. 99.5%). However, a slight decrease could be observed for temperatures higher than 450℃, still with a selectivity of around 98%.

Table 6. Comparison with available data with different types of catalysts over CO_2 methanation at 300℃

Catalysts	Composition*	Reaction conditions		CO_2 Conv.(%)	CH_4 Sel.(%)	Ref.
		H_2/CO_2	GHSV/WHSV			
SBA-15	Ni15	4	10,000 mL/gcat· h	15	62	[94]
MCM-41	Ni15	4	43,000 mL/gcat· h	21	91	[95]
MCM-41	Ni15/Ce15	4	43,000 mL/gcat· h	40	98	
USY	Ni15	4	43,000 mL/gcat· h	20	93	
ZrO_2	Ni15	4	n.m	39	59	[96]
SiO_2	Ni15	4	60,000 mL/gcat· h	55	96	[97]
Meso-γ-Al_2O_3	Ni15	3.5	9,000 mL/gcat· h	46	99	[98]
NMA**	Ni15	4	12,000 h^{-1}	63	99	[55]
	Ni15/La2			75	98	
NMA	Ni15/Cu1	4	12,000 h^{-1}	62	99	[53]
NMA	Ni15/V2	4	12,000 h^{-1}	75	99	[58]
3P-NMA	Ni15	4	12,000 h^{-1}	83.5	99	**This work**

*Ni(wt.%)/Promoter(wt.%)

**NMA- NiMgAl-mixed oxides derived from hydrotalcite catalysts

Table 6 shows the comparison of 3P-NMA to available data in the literature, with different supports and with the same NMA-type but different ways of modification. Among all, 3P-NMA seemed to be the best candidate for CO_2 methanation in terms of CO_2 conversion and CH_4 selectivity.

TOS run was performed at 300°C for 3P-NMA (Figure 10c). CO_2 conversion and CH_4 selectivity are in line with the catalytic test with ca. 81-82% and 99%, respectively. After a 16-hour test, the CH_4 selectivity decreased by ca. 1% while CO_2 conversion remained constant. This excellent stability of the 3P-NMA catalyst provides considerable potential for industrial applications. Moreover, the STY calculations on all catalysts, mmol/g_{cat}.h, led to the following ranking: STY 5P-NMA (0.3) < STY NMA (3.4) < 1P-NMA (9.6) < 3P-NMA (10.4), which was also in accordance with the catalytic test. The highest value was seen on 3P-NMA catalyst. The result of the stability test and the outstanding performance of 3P-NMA at 300°C allows us to point out that such material is a promising catalyst for methanation at a low temperature.

On the other hand, the 5P-NMA clearly showed inferior conversion in all temperature ranges. One can note that CO_2 conversion could be observed at only 60% at 450°C, and its performance was separated from the others (Figure 10a, b). The different behavior may be attributed to the high amount of P123 introduced even though the morphology structure of HT remains intact, as pointed out by the SEM, BET, and XRD results.

Why does the 3P-NMA be the best catalyst system? To understand the better catalytic activity of 3P-NMA, the relationships between CO_2 conversion versus catalyst features will be discussed in this following part of this paper. The correlations are presented in Figures 11a and b.

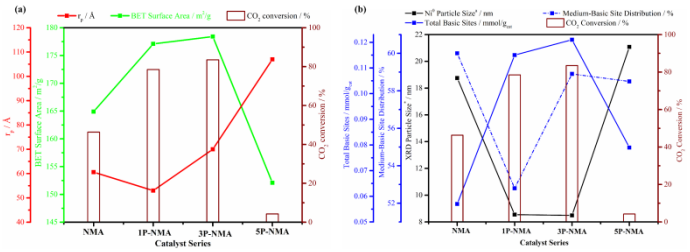

*Calculated from the Scherrer equation at 2θ = 51° on reduced catalysts (Supplementary Table 2).

Figure 11. The correlations of CO_2 conversion (%) at 300°C versus (a) BET surface area (m^2/g) and r_p (nm) and (b) Ni^0 particle size (nm), total basicity (mmol/g_{cat}), and medium basic site distribution (%).

(a)-The catalytic performance in relation to BET surface area and pore size is plotted in Figure 11a to illustrate how structural characteristics impact catalytic performances. It was discovered that adding 1-3wt% resulted in an increase in surface area (from 165 m^2/g to 177 m^2/g and 178 m^2/g, respectively); however, 5P-NMA exhibited a significant decline even when compared to the original NMA. It is required to have a large surface area where the CO_2 molecule could be absorbed and dissociated into intermediates that can subsequently be hydrogenated to yield CH_4. The catalytic tests from our study were found to be in good agreement with measured surface area, 1P123, 3P-NMA having a greater conversion and selectivity than that of NMA, which possess the largest surface area, while 5 wt% P123 was introduced, a substantial decrease in the surface area could be noted, resulted in low performance. Meanwhile, the pore size of the series had been gradually increased in the order of NMA < 1P-NMA < 3P-NMA < 5P-NMA catalysts. As previously discussed, this is most likely owing to a partial blockage of a smaller pore caused by the high concentration of surfactant P123.

(b)-The influences of Ni dispersion and basicity toward CO_2 methanation have been investigated. As shown in Figure 11b, some remarks could be made. In terms of Ni dispersion, an examination of Ni^0 particle size calculated from reduced samples (Supplementary Eq. 1) shows that: 5P-NMA possesses the largest Ni^0 size (L_{Ni0} = 21.08 nm), followed by a smaller size of NMA (L_{Ni0} = 18.75 nm). 1P-NMA and 3P-NMA own relatively small Ni metal particles, more than a half at 8.55 nm and 8.49 nm, respectively. This was demonstrated by TEM results, in which the metallic Ni^0 particle size could be seen at a smaller value (Figure 3, 1B and 2B). Separately, smaller particle size had been reported as a critical parameter to achieve a high catalytic activity toward CO_2 methanation [49, 99, 100]. The results show that the smallest Ni-particle was found on 3P-NMA (see the black line).

Regarding the influence of basicity on catalytic performances, the prevailing opinion was that basic sites facilitate acidic-CO_2 activation and restrict carbon deposition on the catalyst surface, hence enhancing activity and stability. Our results revealed that all P123-containing catalysts had a higher number of basic sites than non-modified hydrotalcite (blue-continuous line), implying that incorporating P123 into the HT-derived framework will generate more basic sites: NMA < 5P-NMA < 1P-NMA < 3P-NMA. The proportions of the medium site (blue-dashed line) on each catalyst, on the other hand, were influenced by the concentration of P123, even though total basicity ranged between 53 and 60%. Although NMA had the least total basicity but the highest share of medium sites, 3P-NMA owned the highest number of basicity with roughly the same percentage of medium sites. As a consequence, the medium site proportions increased in the order of NMA (34 µmol/g_{cat}) < 5P-NMA (47 µmol/g_{cat}) < 1P-NMA (61 µmol/g_{cat}) < 3P-NMA (71 µmol/g_{cat}).

Overall, 5P-NMA possessed a modest number of medium sites, with surface area typically low along with a large crystallite size; this explained the poor performance compared to the others. 3P-NMA, on the contrary, exhibited the best catalytic activity with the highest surface area, the smallest Ni^0 particle size and the highest amount of medium-basic site properties (see Table 7), in particular the presence of bidentate species that was found to be relatively huge on 3P-NMA at 250-350°C.

Table 7. Summarized properties of xP-NMA catalysts dedicated to different behaviors

3P-NMA	5P-NMA
smallest Ni^0 particle size	largest Ni^0 particle size
largest surface area	lowest surface area
the highest number of medium basic site	low amount of medium basicity
best catalytic performance	poor catalytic activity

3.3. *Operando* FTIR measurement results at 300°C

With regarding the catalytic activity of all catalysts in the previous section, it was discovered that the best candidate at 300°C is 3P-NMA; hence, *Operando* FTIR tests were carried out at the same temperature for the parent-NMA and 3P-NMA to further understand the rationale. This section will discuss the *Operando* FTIR observations of NMA and 3P-NMA in gas-phase and catalyst surface, sequentially.

3.3.1. Gas-phase diagnostic

Conventional *Operando* FT-IR spectroscopy analysis in the range of 4000-950 cm^{-1} was implemented to identify the gas-phase compounds during the CO_2 hydrogenation reaction. The results of CO_2 adsorption and methanation at 300°C are illustrated in Figure 12.

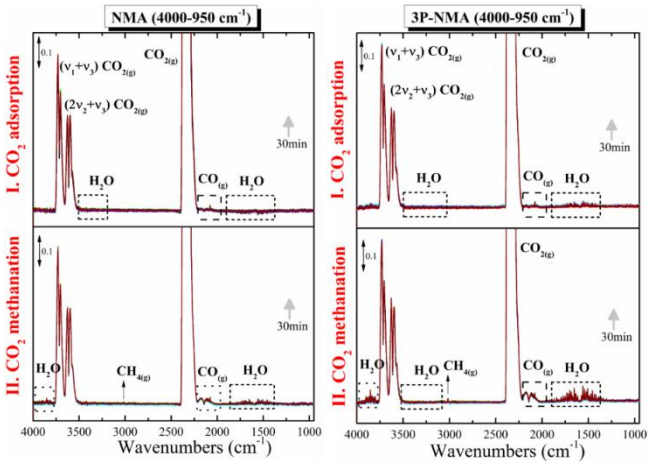

Figure 12. *Operando* FTIR gas-phase diagnostic on NMA and 3PNMA catalysts (full range)

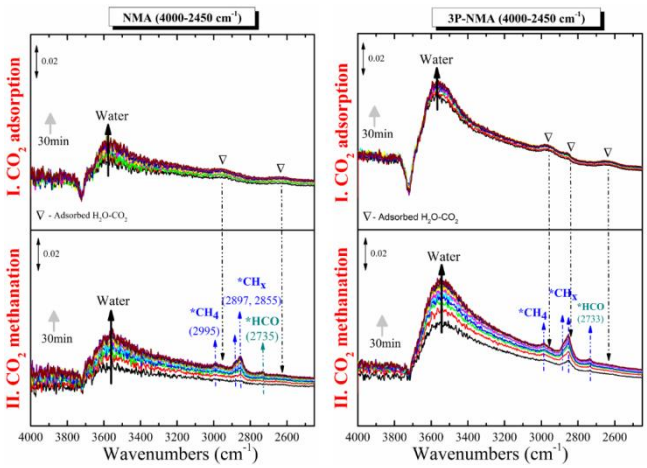

Figure 13. Surface *Operando*-FTIR results of NMA and 3P-NMA catalysts in the 4000-2450 cm^{-1} range during I. CO_2 adsorption and II. CO_2 methanation

Figure 12 depicts the emergence of all bands in the gas phase during CO_2 adsorption and CO_2 methanation studies ($CO_{2(g)}$, $CO_{(g)}$ [88-91], $H_2O_{(g)}$ [91, 101], and $CH_{4(g)}$ [102, 103]).

CO_2 was dissociated into CO in both conditions owing to the presence of Ni as active sites. During methanation monitoring, a CO signal (ground state) was found between 2165 and 2120 cm^{-1} [91], along with methane [103] (3015 cm^{-1}) and water generated. The results also showed that such bands were visible at higher intensities on 3P-NMA than on NMA, implying that methane production was stimulated more effectively on 3P-NMA.

3.3.2. Catalyst surface diagnostic

As illustrated in Figure 13 and 14, the subtracted spectra on the surface of catalysts are given in two wavenumber ranges: 4000-2450 cm^{-1} and 2450-950 $cm^{-1,}$ respectively. All band intensities increased immediately after reactant injection and became stable after ca. 30 min.

In the range of 4000-2450 cm^{-1} wavenumbers **(Figure 13):** The CO_2 adsorption spectra on both catalysts differed in appearance and band intensity, as seen in Figure 13. The identifications of all bands during CO_2 adsorption and CO_2 methanation were also made [101, 104-107].

General observations:

- Water (*HOH species) 3600-3700 cm^{-1} was released during CO_2 adsorption as a result of catalyst reduction [101, 107] and during CO_2 methanation as a product for both catalysts.
- Under methanation conditions, the C-H stretching vibrations of $*CH_4$ were observed at 2995 cm^{-1} and 3015 cm^{-1} [103, 104], respectively, while the C-H stretching vibration from *HCOO (CH_x species) was attributed to small bands at 2897 cm^{-1} and 2855 cm^{-1} [104] was seen on both catalyst surfaces.
- Furthermore, the 2735 cm^{-1} IR band combined with the 1763 cm^{-1} band might be ascribed to aldehyde hydrogen *HCO species (formyl) [105, 106], which has received less recognition in the literature in terms of *IR* measurement

In terms of differences in catalytic behaviors, while absorbed H_2O-CO_2 (∇) was detected at a greater intensity on 3P-NMA with three-adsorbed species, the parent-NMA clearly displayed only two equivalent bands at a lower intensity during CO_2 adsorption studies. Besides this, all band intensities were seen at a higher level on 3P-NMA under both adsorption and methanation conditions. Overall, the *Operando* adsorption and methanation data validated the promotional effect of adding P123 to the NMA catalyst by enhancing adsorption capacity, which coincided with the CO_2-TPD results and *in-situ* CO_2 adsorption investigations.

In the 2450-950 cm^{-1} range **(Figure 14):** To be able to get insight into species diversification, arrows with distinct meanings were used, with the direction of the arrow symbolizing the increase or collapse of bands, and bolder and thinner arrows suggesting stronger and weaker changes, respectively. The various tints, on the other hand, reflected various species (the blue arrow - formate, methane, and CHx species, the black arrow - water, dark-green arrows - formyl, and the pink arrow - all carbonate species).

But first and foremost, it should be emphasized that the *operando* measurement was carried out with flow settings, unlike *in-situ* measurements at static conditions, which led

to certain band position shifts. Two bands, for example, were visible in *Operando* but not in the *in-situ* analysis ($CO_{(ad)}$ 1992 and 1811 cm^{-1}) (cf. Figure 9 left, CO_2 adsorption behaviors). This event occurred because such species were adsorbed and maintained on the catalyst surface under static conditions; nevertheless, they were peeled/flushed from the surface under flowing conditions, resulting in a change of such positions. A similar situation was observed for carbonate species, with a little change in band location in the 1670-950 cm^{-1} wavenumbers. Figure 14 depicts the results, which include positions and assignments for all bands [26, 87-90, 103, 104].

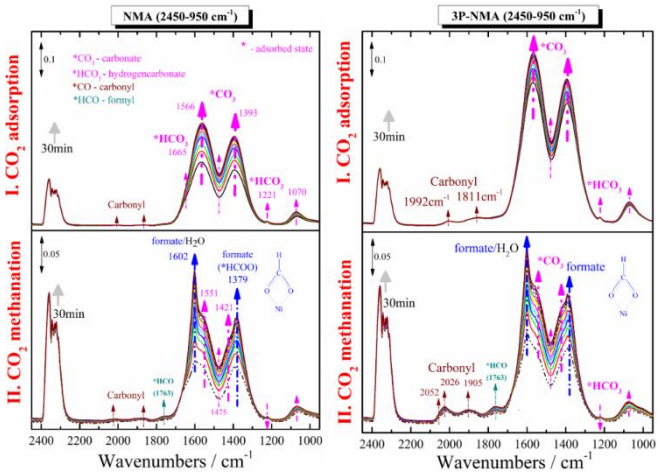

Figure 14. Surface *Operando*-FTIR results of NMA and 3P-NMA catalysts in the 2450-950 cm^{-1} range during I. CO_2 adsorption, and II. CO_2 methanation

During CO_2 adsorption conditions:

- All carbonyl (*CO) IR bands were discovered for both catalysts.
- Carbonate species seemed to prevail in 3P-NMA in both CO_2 adsorption and CO_2 methanation experiments.

Under CO_2 methanation conditions:

- Hydrogen carbonate ($*HCO_3$) and carbonate ($*CO_3$) species were evident in all cases [103, 106].
- The appearance of the bands at 2052 cm^{-1}, 2026 cm^{-1}, and 1905 cm^{-1} corresponded to the carbonyl species at 2086 cm^{-1}, 2067 cm^{-1}, and 1903 cm^{-1} from *in-situ* CO_2 sorption measurements, which were displaced under the flowing situation as discussed.
- While hydrogen-carbonate species were thought to originate from the surface-OH (*OH) group, where it could function as weak-basic sites, Di Cosimo et al. [26] proposed that oxygen from M^{n+}-O^{2-} pairs (medium basic site) was interacted with CO_2 to generate $*CO_3$ species. Carbonate species would be further hydrogenated on the catalyst surface to produce methane.

Additionally, the emergence of the band at 1763 cm^{-1} (formyl, $HCO^-_{(ad)}$) during methanation (which was not found during *Operando* CO_2 adsorption) suggests that the mechanism may follow a pathway that involves formyl as an intermediate [106, 108]. The mechanism involving formyl, therefore, could be described as follows: carbonate/hydrogen carbonate → formyl → formate → methane.

Note that carbonate and formate species were observed with considerably higher intensity on 3P-NMA than on NMA. On 3P-NMA, CO_2 adsorption and conversion were accelerated, allowing for the formation of formate intermediates as well as an increase in CO_2 methanation yield under the same working conditions.

Based on *in-situ*, *operando*, and CO_2-TPD measurements, we preliminary proposed a mechanism of CO_2 methanation on the 3P-NMA catalyst with regard to [106, 108]. CO_2 has been considered as a Lewis acid, with carbon atom lingering in the center due to its low electronegativity ($O^{\delta-} = C^{\delta+} = O^{\delta-}$). As a result, the transformation of CO_2 necessitates the use of a catalyst having basic sites where it can be absorbed and subsequently transformed (see Figure 15).

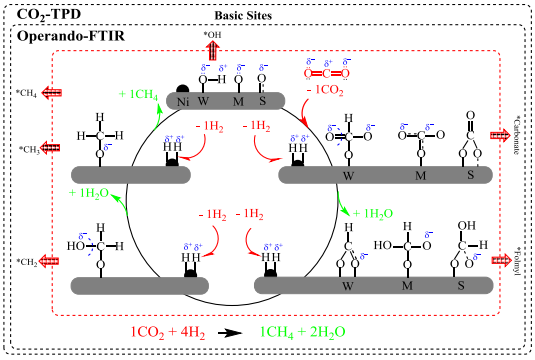

Figure 15. Proposed mechanism of CO_2 methanation over 3P-NMA

Carbon dioxide molecules adsorbed dominantly on the catalyst surface at weak and medium sites (as evidenced by CO_2-TPD measurements) resulted in the formation of several carbonate species (demonstrated by both *in-situ* and *Operando* experiments). Hydrogen was spent in four-consecutive phases to hydrogenate such carbonate species to formyl species (detected by *Operando* FTIR measurements under methanation conditions) and further to CH_x and lastly CH_4, completing one cycle. One molecule of CO_2 and four molecules of H_2 were consumed (presented in red) to produce 1 molecule of CH_4, and $2H_2O$ molecules (in green) are the total count for one cycle.

3.4. Evaluations of spent catalysts

3.4.1. X-ray diffraction results

The WAXD results of all catalysts after the thermal reaction are shown in Figure 16. As presented, there was no diffraction peak detected at $2\theta = 26.6°$, which is associated with graphitic carbon formation [109]; therefore, we can rule out C-deposition on all of our catalysts.

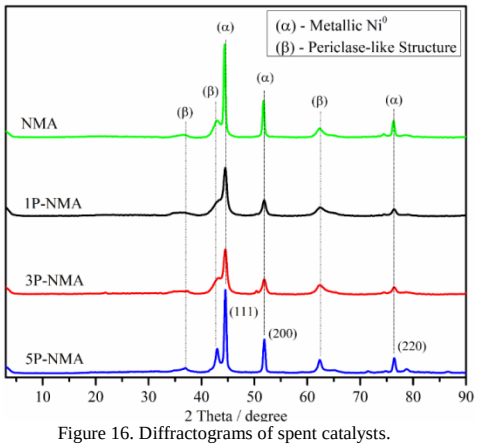

Figure 16. Diffractograms of spent catalysts.

The reflections confirmed the presence of metallic nickel phase (α-phase) at 2θ ca. 44.5°, 51°, and 76°, corresponding to crystal planes of (111), (200) and (220), respectively. Meanwhile, the diffractions at 2θ ca. 36.7°, 43° and 62.5° were observed (β-phase), which were also reported elsewhere on the same NiMgAl-HT materials [71, 72]. They correspond to the mixed oxides obtained after the thermal treatment of double-layered hydroxides. Interestingly, the intensities of β-phase were sharper and more intense for 5P-NMA, suggesting that the existence of periclase-like structure was more intact in 5P-NMA; in other words, stronger Ni-HT matrix interactions were proved, in accordance with H_2-TPR results. The latter showed lower intensities of diffraction peaks and broader bands.

The size of Ni metal crystallites was determined using the Scherrer equation from the 2θ diffraction peak at approx. 51° corresponding to the (200) crystal plane of Ni^0, data can be found in Supplementary Table 2. Nickel crystallite size decreased from ca. 18.75 nm for the NMA to ca. 8.55 nm and 8.49 nm for 1P-NMA and 3P-NMA due to the promotion of P123. However, the value obtained for 5P-NMA was higher than a non-modified catalyst, i.e., 21.08 nm, respectively. It seems that 5 wt% P123 negatively affected the size of Ni-metal size.

The Ni metal particle did not increase after the test, but decreased for all catalysts except 1P-NMA, which showed a minor change. The possibility of re-dispersed Ni^0 occurring after the reaction that resulted in a decrease in Ni^0 after the experiments could be pointed out. In this case, the sintering of active sites after the thermal reaction could be suppressed. Possibly, the sintering of active sites was then re-oxidized by highly active oxygen on the framework of mix-oxides, resulting in the re-dispersion of metals on the surface under operating temperature conditions.

3.4.2. TG measurements

In our results, two regions of weight loss could be seen: the first occurred near room temperature in the flow of synthetic air, which was due to the drying step with about 0.7-1.4% weight loss. The negative peaks could clearly see with a loss of ca. 4.1%, 4.8%, 3.9% and 3.6 wt% corresponding to NMA, 1P-NMA, 3P-NMA and 5P-NMA, respectively, from 180 to 250℃ due to the removal of water in the framework.

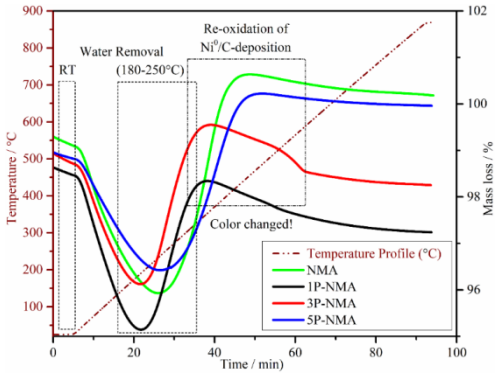

Figure 17. TG profiles of catalyst series

A slight increase of the curve between 350-460℃ was observed. This gain suggested either the existence of C-deposition or the re-oxidation of Ni to NiO or both scenarios. No C-deposition was observed in the association with XRD measurements of spent catalysts. Besides, the color of catalysts had been turned into light green (precursor NiO color) during the TG measurement. These revealed that catalysts were re-oxidized during the methanation reaction. In the latter case, the removal rate of water was slower than the re-oxidation of Ni in mixed-oxide catalysts. This suggested us the positive peaks obtained at 350-460℃ have mainly belonged to the transformation of Ni into NiO. This was also stated by Dias [97], where the spent catalysts were examined after CO_2 methanation was performed over Ni-Cu/SiO_2 catalyst. Overall, our catalysts demonstrated a high C-deposition tolerance.

4. Conclusions

In this study, hydrotalcite-derived catalysts were modified by a novel method with surfactant Pluronic P123- the structural template of SBA-15: Incorporating P123 to modify the morphology and properties of hydrotalcite-derived materials, instead of adding a second metal - which is currently the most common way. The results turned out to be promising, with excellent stability and selectivity towards CH_4 at a lower temperature.

After calcination, P123 was removed, leaving the modification in the structure of catalysts while maintaining the intrinsic characteristics of the catalyst. The SEM images indicated a complete transformation in the morphology of catalysts containing P123 from solid into soft and porous phases. The N_2-sorption revealed a change in isotherm plots in which more layers were observed with catalysts containing surfactant; the highest surface area of 178 m^2/g belonging to 3P-NMA against 165 m^2/g of non-modified catalyst. Furthermore, we observed that adding P123 also enlarged the pore size of parent hydrotalcite. Wide-angle X-ray diffraction, together with H_2-TPR and CO_2-TPD, the structure of HT-derived catalysts was carried out without distortion, the layer structure after the modification has been preserved. The existence of readily and hardly reducible Nikel-species also affected the catalytic performance of the catalysts. It can be said that using P123 during the synthesis step rebuilt the NiMgAlOx catalysts.

In-situ CO_2 sorption investigation at working temperatures revealed the presence of unidentate, bidentate (chelating and bridging), and tridentate carbonate on the catalyst surface after CO_2 adsorption. The relationship between these species and related weak, medium, and strong basic sites in CO_2-TPD was proposed.

By adjusting the chemical portion of P123 at 3wt%, the catalyst displayed a remarkable low-temperature performance in CO_2 conversion at 83.5% with almost 99.5% CH_4 selectivity at 300°C. The appropriate combination of high surface area, small Ni^0 particle size, well-dispersed Ni, and a large amount of weak-medium basic site was found on 3P-NMA.

Operando experiments at 300°C demonstrated that 3P-NMA could facilitate CO_2 adsorption in the metal-oxide pair more than the generation of surface OH. As a result, the basicity of NiMgAl-oxide was enhanced. Experimentally, it was a strong indication that the mechanism might concern *HCO as a key intermediate following CH_x and CH_4 formation.

Finally, there is a potential for applying the same methodology with various metals to synthesize a proper catalyst for a particular reaction and to scale up the procedure for industrial application in environmental catalysis.

Acknowledgments

This work has received support from the European Research Framework Program: H2020 | Marie Skłodowska-Curie Action (MSCA), PIONEER project: plasma catalysis for CO_2 recycling (Grant no. 813393).

The part of research results presented in this paper has been developed with the use of equipment financed from the funds of the "Excellence Initiative - Research University" program at AGH University of Science and Technology.

The authors would like to thank Prof. Świerczek for evaluating TG on spent catalysts (AGH University of Science and Technology, Poland), and Prof. Jaafar (LCS-CNRS, France) for the help with the SEM-EDX operation.

References

[1] NOAA, Recent Global CO2 Trend, National Oceanic and Atmospheric Administration.
[2] D.M. D'Alessandro, B. Smit, J.R. Long, Carbon Dioxide Capture: Prospects for New Materials, Angewandte Chemie International Edition, 49 (2010) 6058-6082. https://doi.org/10.1002/anie.201000431.
[3] P. Nema, S. Nema, P. Roy, An overview of global climate changing in current scenario and mitigation action, Renewable and Sustainable Energy Reviews, 16 (2012) 2329-2336. https://doi.org/10.1016/j.rser.2012.01.044.
[4] X. Xiaoding, J.A. Moulijn, Mitigation of CO2 by Chemical Conversion: Plausible Chemical Reactions and Promising Products, Energy & Fuels, 10 (1996) 305-325. http://doi.org/10.1021/ef9501511.
[5] G. Centi, S. Perathoner, Opportunities and prospects in the chemical recycling of carbon dioxide to fuels, Catalysis Today, 148 (2009) 191-205. https://doi.org/10.1016/j.cattod.2009.07.075.
[6] P. Gabrielli, M. Gazzani, M. Mazzotti, The Role of Carbon Capture and Utilization, Carbon Capture and Storage, and Biomass to Enable a Net-Zero-CO2 Emissions Chemical Industry, Industrial & Engineering Chemistry Research, 59 (2020) 7033-7045. https://doi.org/10.1021/acs.iecr.9b06579.
[7] IEA, Carbon capture, utilisation and storage.,
[8] C. Song, Global challenges and strategies for control, conversion and utilization of CO2 for sustainable development involving energy, catalysis, adsorption and chemical processing, Catalysis Today, 115 (2006) 2-32. https://doi.org/10.1016/j.cattod.2006.02.029.
[9] K. Müller, M. Fleige, F. Rachow, D. Schmeißer, Sabatier based CO2-methanation of Flue Gas Emitted by Conventional Power Plants, Energy Procedia, 40 (2013) 240-248. https://doi.org/10.1016/j.egypro.2013.08.028.
[10] M. Götz, J. Lefebvre, F. Mörs, A. McDaniel Koch, F. Graf, S. Bajohr, R. Reimert, T. Kolb, Renewable Power-to-Gas: A technological and economic review, Renewable Energy, 85 (2016) 1371-1390. https://doi.org/10.1016/j.renene.2015.07.066.
[11] M. Götz, A. Koch, F. Graf, State of the Art and Perspectives of CO2 Methanation Process Concepts for Power-to-Gas Applications, International Gas Research Conference Proceedings, 1 (2014)
[12] D. van der Wiel, J. Zilka, Y. Wang, A. Tonkovich, R. Wegeng, Carbon Dioxide Conversions in Microreactors, Conference: 4th International Conference on Microreaction Technology, (2000)
[13] W. Wei, G. Jinlong, Methanation of carbon dioxide: an overview, Frontiers of Chemical Science and Engineering, 5 (2011) 2-10. https://doi.org/10.1007/s11705-010-0528-3.
[14] M.A.A. Aziz, A.A. Jalil, S. Triwahyono, A. Ahmad, CO2 methanation over heterogeneous catalysts: recent progress and future prospects, Green Chemistry, 17 (2015) 2647-2663. https://doi.org/10.1039/C5GC00119F.
[15] X. Su, J. Xu, B. Liang, H. Duan, B. Hou, Y. Huang, Catalytic carbon dioxide hydrogenation to methane: A review of recent studies, Journal of Energy Chemistry, 25 (2016) 553-565. https://doi.org/10.1016/j.jechem.2016.03.009.
[16] G. Garbarino, D. Bellotti, P. Riani, L. Magistri, G. Busca, Methanation of carbon dioxide on Ru/Al2O3 and Ni/Al2O3 catalysts at atmospheric pressure: Catalysts activation, behaviour and stability, International Journal of Hydrogen Energy, 40 (2015) 9171-9182. https://doi.org/10.1016/j.ijhydene.2015.05.059.
[17] G.D. Weatherbee, C.H. Bartholomew, Hydrogenation of CO2 on group VIII metals: IV. Specific activities and selectivities of silica-supported Co, Fe, and Ru, Journal of Catalysis, 87 (1984) 352-362. https://doi.org/10.1016/0021-9517(84)90196-9.
[18] E. Vesselli, J. Schweicher, A. Bundhoo, A. Frennet, N. Kruse, Catalytic CO2 Hydrogenation on Nickel: Novel Insight by Chemical Transient Kinetics, The Journal of Physical Chemistry C, 115 (2011) 1255-1260. https://doi.org/10.1021/jp106551r.
[19] G.D. Weatherbee, C.H. Bartholomew, Hydrogenation of CO2 on group VIII metals: I. Specific activity of NiSiO2, Journal of Catalysis, 68 (1981) 67-76. https://doi.org/10.1016/0021-9517(81)90040-3.
[20] S. Rönsch, J. Schneider, S. Matthischke, M. Schlüter, M. Götz, J. Lefebvre, P. Prabhakaran, S. Bajohr, Review on methanation – From fundamentals to current projects, Fuel, 166 (2016) 276-296. https://doi.org/10.1016/j.fuel.2015.10.111.
[21] A. Beuls, C. Swalus, M. Jacquemin, G. Heyen, A. Karelovic, P. Ruiz, Methanation of CO2: Further insight into the mechanism over Rh/γ-Al2O3 catalyst, Applied Catalysis B: Environmental, 113-114 (2012) 2-10. https://doi.org/10.1016/j.apcatb.2011.02.033.
[22] W. Gac, W. Zawadzki, M. Rotko, M. Greluk, G. Słowik, G. Kolb, Effects of support composition on the performance of nickel catalysts in CO2 methanation reaction, Catalysis Today, 357 (2020) 468-482. https://doi.org/10.1016/j.cattod.2019.07.026.
[23] P. Frontera, A. Macario, M. Ferraro, P. Antonucci, Supported Catalysts for CO2 Methanation: A Review, Catalysts, 7 (2017). https://doi.org/10.3390/catal7020059.
[24] J. Martínez, E. Hernández, S. Alfaro, R. López Medina, G. Valverde Aguilar, E. Albiter, M.A. Valenzuela, High Selectivity and Stability of Nickel Catalysts for CO2 Methanation: Support Effects, Catalysts, 9 (2019). https://doi.org/10.3390/catal9010024.
[25] A.S. Russell, C.N. Cochran, Alumina Surface Area Measurements, Industrial & Engineering Chemistry, 42 (1950) 1332-1335. https://doi.org/10.1021/ie50487a024.
[26] J.I. Di Cosimo, V.K. Díez, M. Xu, E. Iglesia, C.R. Apesteguía, Structure and Surface and Catalytic Properties of Mg-Al Basic Oxides, Journal of Catalysis, 178 (1998) 499-510. https://doi.org/10.1006/jcat.1998.2161.
[27] D. Hu, J. Gao, Y. Ping, L. Jia, P. Gunawan, Z. Zhong, G. Xu, F. Gu, F. Su, Enhanced Investigation of CO Methanation over Ni/Al2O3 Catalysts for Synthetic Natural Gas Production, Industrial & Engineering Chemistry Research, 51 (2012) 4875-4886. https://doi.org/10.1021/ie300049f.
[28] D. Pandey, G. Deo, Effect of support on the catalytic activity of supported Ni–Fe catalysts for the CO2 methanation reaction, Journal of Industrial and Engineering Chemistry, 33 (2016) 99-107. https://doi.org/10.1016/j.jiec.2015.09.019.
[29] J.-N. Park, E.W. McFarland, A highly dispersed Pd–Mg/SiO2 catalyst active for methanation of CO2, Journal of Catalysis, 266 (2009) 92-97. https://doi.org/10.1016/j.jcat.2009.05.018.
[30] Q. Pan, J. Peng, T. Sun, S. Wang, S. Wang, Insight into the reaction route of CO2 methanation: Promotion effect of medium basic sites, Catalysis Communications, 45 (2014) 74-78. https://doi.org/10.1016/j.catcom.2013.10.034.
[31] N.A. Sholeha, S. Mohamad, H. Bahruji, D. Prasetyoko, N. Widiastuti, N.A. Abdul Fatah, A.A. Jalil, Y.H. Taufiq-Yap, Enhanced CO2 methanation at mild temperature on Ni/zeolite from kaolin: effect of metal–support interface, RSC Advances, 11 (2021) 16376-16387. https://doi.org/10.1039/D1RA01014J.
[32] D. Lorito, H. Li, A. Travert, F. Maugé, F.C. Meunier, Y. Schuurman, C. Mirodatos, Understanding deactivation processes during bio-syngas methanation: DRIFTS and SSITKA experiments and kinetic modeling over Ni/Al2O3 catalysts, Catalysis Today, 299 (2018) 172-182. https://doi.org/10.1016/j.cattod.2017.06.041.
[33] G. Tang, D. Gong, H. Liu, L. Wang, Highly Loaded Mesoporous Ni–La2O3 Catalyst Prepared by Colloidal Solution Combustion Method for CO2 Methanation, Catalysts, 9 (2019). https://doi.org/10.3390/catal9050442.
[34] S. Tada, T. Shimizu, H. Kameyama, T. Haneda, R. Kikuchi, Ni/CeO2 catalysts with high CO2 methanation activity and high CH4 selectivity at low temperatures, International Journal of Hydrogen Energy, 37 (2012) 5527-5531. https://doi.org/10.1016/j.ijhydene.2011.12.122.
[35] R. Razzaq, H. Zhu, L. Jiang, U. Muhammad, C. Li, S. Zhang, Catalytic Methanation of CO and CO2 in Coke Oven Gas over Ni–Co/ZrO2–CeO2, Industrial & Engineering Chemistry Research, 52 (2013) 2247-2256. https://doi.org/10.1021/ie301399z.
[36] X. Jia, X. Zhang, N. Rui, X. Hu, C.-j. Liu, Structural effect of Ni/ZrO2 catalyst on CO2 methanation with enhanced activity, Applied Catalysis B: Environmental, 244 (2019) 159-169. https://doi.org/10.1016/j.apcatb.2018.11.024.
[37] W. Zhen, B. Li, G. Lu, J. Ma, Enhancing catalytic activity and stability for CO2 methanation on Ni@MOF-5 via control of active species dispersion, Chemical Communications, 51 (2015) 1728-1731. https://doi.org/10.1039/C4CC08733J.
[38] Y. Feng, W. Yang, W. Chu, A Study of CO₂ Methanation over Ni-Based Catalysts Supported by CNTs with Various Textural Characteristics, International Journal of Chemical Engineering, 2015 (2015) 795386. https://doi.org/10.1155/2015/795386.
[39] S. Nishimura, A. Takagaki, K. Ebitani, Characterization, synthesis and catalysis of hydrotalcite-related materials for highly efficient materials transformations, Green Chemistry, 15 (2013) 2026-2042. https://doi.org/10.1039/C3GC40405F.
[40] T. Zhao, X. Hu, Y. Wu, Z. Zhang, Hydrogenation of CO2 to Formate with H2: Transition Metal Free Catalyst Based on a Lewis Pair, Angewandte Chemie International Edition, 58 (2019) 722-726. https://doi.org/10.1002/anie.201809634.
[41] Z. Li, R. Shi, J. Zhao, T. Zhang, Ni-based catalysts derived from layered-double-hydroxide nanosheets for efficient photothermal CO2 reduction under flow-type system, Nano Research, 14 (2021) 4828-4832. https://doi.org/10.1007/s12274-021-3436-6.
[42] J. Feng, Y. He, Y. Liu, Y. Du, D. Li, Supported catalysts based on layered double hydroxides for catalytic oxidation and hydrogenation: general functionality and promising application prospects, Chemical Society Reviews, 44 (2015) 5291-5319. https://doi.org/10.1039/C5CS00268K.
[43] Q. Wang, D. O'Hare, Recent Advances in the Synthesis and Application of Layered Double Hydroxide (LDH) Nanosheets, Chemical Reviews, 112 (2012) 4124-4155. https://doi.org/10.1021/cr200434v.
[44] A. Vaccari, Preparation and catalytic properties of cationic and anionic clays, Catalysis Today, 41 (1998) 53-71. https://doi.org/10.1016/S0920-5861(98)00038-8.
[45] M. Nguyen-Quang, F. Azzolina-Jury, B. Samojeden, M. Motak, P. Da Costa, On the influence of the preparation routes of NiMgAl-mixed oxides derived from hydrotalcite on their CO2 methanation catalytic activities, International Journal of Hydrogen Energy, (2022). https://doi.org/10.1016/j.ijhydene.2022.08.278.
[46] F. Cavani, F. Trifirò, A. Vaccari, Hydrotalcite-type anionic clays: Preparation, properties and applications, Catalysis Today, 11 (1991) 173-301. https://doi.org/10.1016/0920-5861(91)80068-K.
[47] C. Forano, U. Costantino, V. Prévot, C.T. Gueho, Chapter 14.1 - Layered Double Hydroxides (LDH), Developments in Clay Science, 5 (2013) 745-782. https://doi.org/10.1016/B978-0-08-098258-8.00025-0.
[48] S. Miyata, Anion-Exchange Properties of Hydrotalcite-Like Compounds, Clays and Clay Minerals, 31 (1983) 305-311. https://doi.org/10.1346/CCMN.1983.0310409.
[49] C. Asmelash, F. Krebs, S. Perathoner, S. Abate, G. Centi, R. Palkovits, Hydrotalcite based Ni-Fe/(Mg, Al)O:X catalysts for CO2 methanation-tailoring Fe content for improved CO dissociation, basicity, and particle size, Catalysis Science & Technology, 8 (2018). https://doi.org/10.1039/C7CY02099F.
[50] A. Chatla, F. Abu-Rub, A.V. Prakash, G. Ibrahim, N.O. Elbashir, Highly stable and coke-resistant Zn-modified Ni-Mg-Al hydrotalcite derived catalyst for dry reforming of methane: Synergistic effect of Ni and Zn, Fuel, 308 (2022) 122042. https://doi.org/10.1016/j.fuel.2021.122042.
[51] P. Summa, K. Świrk, D. Wierzbicki, M. Motak, I. Alxneit, M. Rønning, P. Da Costa, Co-Precipitated Ni-Mg-Al Hydrotalcite-Derived Catalyst Promoted with Vanadium for CO2 Methanation, Molecules, 26 (2021). https://doi.org/10.3390/molecules26216506.
[52] A.I. Tsiotsias, N.D. Charisiou, I.V. Yentekakis, M.A. Goula, Bimetallic Ni-Based Catalysts for CO2 Methanation: A Review, Nanomaterials, 11 (2021). https://doi.org/10.3390/nano11010028.
[53] P. Summa, B. Samojeden, M. Motak, D. Wierzbicki, I. Alxneit, K. Świerczek, P. Da Costa, Investigation of Cu promotion effect on hydrotalcite-based nickel catalyst for CO2 methanation, Catalysis Today, 384-386 (2022) 133-145. https://doi.org/10.1016/j.cattod.2021.05.004.

[54] C. Sun, K. Świrk, D. Wierzbicki, M. Motak, T. Grzybek, P. Da Costa, On the effect of yttrium promotion on Ni-layered double hydroxides-derived catalysts for hydrogenation of CO2 to methane, International Journal of Hydrogen Energy, 46 (2021) 12169-12179. https://doi.org/10.1016/j.ijhydene.2020.03.202.
[55] D. Wierzbicki, R. Debek, M. Motak, T. Grzybek, M.E. Gálvez, P. Da Costa, Novel Ni-La-hydrotalcite derived catalysts for CO2 methanation, Catalysis Communications, 83 (2016) 5-8. https://doi.org/10.1016/j.catcom.2016.04.021.
[56] L. Yin, X. Chen, M. Sun, B. Zhao, J. Chen, Q. Zhang, P. Ning, Insight into the role of Fe on catalytic performance over the hydrotalcite-derived Ni-based catalysts for CO2 methanation reaction, International Journal of Hydrogen Energy, (2021). https://doi.org/10.1016/j.ijhydene.2021.12.057.
[57] J. Martins, A.C. Faria, M. Soria, C.V. Miguel, A.E. Rodrigues, L.J.C. Madeira, CO2 Methanation over Hydrotalcite-Derived Nickel/Ruthenium and Supported Ruthenium Catalysts, 9 (2019) 1008. https://doi.org/10.3390/catal9121008.
[58] K. Świrk, P. Summa, D. Wierzbicki, M. Motak, P. Da Costa, Vanadium promoted Ni(Mg,Al)O hydrotalcite-derived catalysts for CO2 methanation, International Journal of Hydrogen Energy, (2021). https://doi.org/10.1016/j.ijhydene.2021.02.172.
[59] J. Wang, H. Ge, W. Bao, Synthesis and characteristics of SBA-15 with thick pore wall and high hydrothermal stability, Materials Letters, 145 (2015). https://doi.org/10.1016/j.matlet.2015.01.113.
[60] P. Hongmanorom, J. Ashok, G. Zhang, Z. Bian, M.H. Wai, Y. Zeng, S. Xi, A. Borgna, S. Kawi, Enhanced performance and selectivity of CO2 methanation over phyllosilicate structure derived Ni-Mg/SBA-15 catalysts, Applied Catalysis B: Environmental, 282 (2021) 119564. https://doi.org/10.1016/j.apcatb.2020.119564.
[61] L. He, Q. Lin, Y. Liu, Y. Huang, Unique catalysis of Ni-Al hydrotalcite derived catalyst in CO2 methanation: cooperative effect between Ni nanoparticles and a basic support, Journal of Energy Chemistry, 23 (2014) 587-592. https://doi.org/10.1016/S2095-4956(14)60144-3.
[62] F. Cavani, F. Trifiró, A.J.C.T. Vaccari, Hydrotalcite-type anionic clays: Preparation, properties and applications, 11 (1991) 173-301. https://doi.org/10.1016/0920-5861(91)80068-K.
[63] G.J. Janz, S.C. Wait, Space- Time Yield and Reaction Rate, The Journal of Chemical Physics, 23 (1955) 1550-1551. 10.1063/1.1742359.
[64] M. Boudart, A. Delbouille, J.A. Dumesic, S. Khammouma, H. Topsøe, Surface, catalytic and magnetic properties of small iron particles: I. Preparation and characterization of samples, Journal of Catalysis, 37 (1975) 486-502. https://doi.org/10.1016/0021-9517(75)90184-0.
[65] T. Lesage, C. Verrier, P. Bazin, J. Saussey, M. Daturi, Studying the NO-trap mechanism over a Pt-Rh/Ba/Al2O3 catalyst by operando FT-IR spectroscopy, Physical Chemistry Chemical Physics, 5 (2003) 4435-4440. https://doi.org/10.1039/B305874N.
[66] B. Wiyantoko, P. Kurniawati, T.E. Purbaningtias, I. Fatimah, Synthesis and Characterization of Hydrotalcite at Different Mg/Al Molar Ratios, Procedia Chemistry, 17 (2015) 21-26. https://doi.org/10.1016/j.proche.2015.12.115.
[67] J. Török, J. Halász, Z. Kónya, P. Sipos, I. Palinko, Mixed Oxides Without Added Noble Metals Derived from Layered Double Hydroxides of the Hydrotalcite Type in the Hydrodechlorination Reaction of Trichloroethylene, Catalysis Letters, 147 (2017) 1-10. https://doi.org/10.1007/s10562-017-2203-5.
[68] Z. Taherian, V. Shahed Gharahshiran, A. Khataee, Y. Orooji, Anti-coking freeze-dried NiMgAl catalysts for dry and steam reforming of methane, Journal of Industrial and Engineering Chemistry, 103 (2021) 187-194. https://doi.org/10.1016/j.jiec.2021.07.032.
[69] D. Wierzbicki, M. Motak, T. Grzybek, M.E. Gálvez, P. Da Costa, The influence of lanthanum incorporation method on the performance of nickel-containing hydrotalcite-derived catalysts in CO2 methanation reaction, Catalysis Today, 307 (2018) 205-211. https://doi.org/10.1016/j.cattod.2017.04.020.
[70] A. Rodrigues, C. Henriques, J. Monteiro, Influence of Ni content on physico-chemical characteristics of Ni, Mg, Al-Hydrotalcite like compounds, Materials Research, 6 (2003). https://doi.org/10.1590/S1516-14392003000400024.
[71] K. Świrk, M. Motak, T. Grzybek, M. Rønning, P. Da Costa, Effect of low loading of yttrium on Ni-based layered double hydroxides in CO2 reforming of CH4, Reaction Kinetics, Mechanisms and Catalysis, 126 (2018). https://doi.org/10.1007/s11144-018-1515-9.
[72] K. Świrk, M.E. Gálvez, M. Motak, T. Grzybek, M. Rønning, P. Da Costa, Dry reforming of methane over Zr- and Y-modified Ni/Mg/Al double-layered hydroxides, Catalysis Communications, 117 (2018) 26-32. https://doi.org/10.1016/j.catcom.2018.08.024.
[73] O.D. Pavel, D. Tichit, I.-C. Marcu, Acido-basic and catalytic properties of transition-metal containing Mg–Al hydrotalcites and their corresponding mixed oxides, Applied Clay Science, 61 (2012) 52–58. https://doi.org/10.1016/j.clay.2012.03.006.
[74] A. Vaccari, Layered double hydroxides: present and future: V. Rives (Ed.), Nova Science Publishers, Inc., New York, 2001, IX+439 pp., ISBN 1-59033-060-9, Applied Clay Science, 22 (2002) 75–76. https://doi.org/10.1016/S0169-1317(02)00112-6.
[75] O.W. Perez-Lopez, A. Senger, N.R. Marcilio, M.A. Lansarin, Effect of composition and thermal pretreatment on properties of Ni–Mg–Al catalysts for CO2 reforming of methane, Applied Catalysis A: General, 303 (2006) 234-244. https://doi.org/10.1016/j.apcata.2006.02.024.
[76] D. Tichit, F. Medina, B. Coq, R. Dutartre, Activation under oxidizing and reducing atmospheres of Ni-containing layered double hydroxides, Applied Catalysis A: General, 159 (1997) 241-258. https://doi.org/10.1016/S0926-860X(97)00085-9.
[77] G. Fornasari, M. Gazzano, D. Matteuzzi, F. Trifirò, A. Vaccari, Structure and reactivity of high-surface-area Ni/Mg/Al mixed oxides, Applied Clay Science, 10 (1995) 69-82. https://doi.org/10.1016/0169-1317(95)00022-V.
[78] N. Ichikuni, D. Murata, S. Shimazu, T. Uematsu, Promoting effect of NiAl2O4 for supported Ni particles on sprayed Ni/Al2O3 catalysts, Catalysis Letters, 69 (2000) 33-36. https://doi.org/10.1023/A:1019009620601.
[79] N. Ichikuni, D. Murata, S. Shimazu, T. Uematsu, Promoting effect of NiAl2O4 for supported Ni particles on sprayed Ni/Al2O3 catalysts, Catalysis Letters - CATALYSIS LETT, 69 (2000) 33-36. 10.1023/A:1019009620601.
[80] F. Prinetto, G. Ghiotti, R. Durand, D. Tichit, Investigation of Acid−Base Properties of Catalysts Obtained from Layered Double Hydroxides, The Journal of Physical Chemistry B, 104 (2000) 11117-11126. https://doi.org/10.1021/jp002715u.
[81] J.C. Lavalley, Infrared spectrometric studies of the surface basicity of metal oxides and zeolites using adsorbed probe molecules, Catalysis Today, 27 (1996) 377-401. https://doi.org/10.1016/0920-5861(95)00161-1.
[82] D.Y. Kalai, K. Stangeland, H. Li, Z. Yu, The effect of La on the hydrotalcite derived Ni catalysts for dry reforming of methane, Energy Procedia, 142 (2017) 3721-3726. https://doi.org/10.1016/j.egypro.2017.12.267.
[83] R. Dębek, M. Radlik, M. Motak, M.E. Galvez, W. Turek, P. Da Costa, T. Grzybek, Ni-containing Ce-promoted hydrotalcite derived materials as catalysts for methane reforming with carbon dioxide at low temperature – On the effect of basicity, Catalysis Today, 257 (2015) 59-65. https://doi.org/10.1016/j.cattod.2015.03.017.
[84] D. Wierzbicki, R. Baran, R. Dębek, M. Motak, M.E. Gálvez, T. Grzybek, P. Da Costa, P. Glatzel, Examination of the influence of La promotion on Ni state in hydrotalcite-derived catalysts under CO2 methanation reaction conditions: Operando X-ray absorption and emission spectroscopy investigation, Applied Catalysis B: Environmental, 232 (2018) 409-419. https://doi.org/10.1016/j.apcatb.2018.03.089.
[85] A. Corma, V. Fornés, R.M. Martín-Aranda, F. Rey, Determination of base properties of hydrotalcites: Condensation of benzaldehyde with ethyl acetoacetate, Journal of Catalysis, 134 (1992) 58-65. https://doi.org/10.1016/0021-9517(92)90209-Z.
[86] F. Prinetto, G. Ghiotti, P. Graffin, D. Tichit, Synthesis and characterization of sol–gel Mg/Al and Ni/Al layered double hydroxides and comparison with co-precipitated samples, Microporous and Mesoporous Materials, 39 (2000) 229-247. https://doi.org/10.1016/S1387-1811(00)00197-9.
[87] G. Busca, V. Lorenzelli, Infrared spectroscopic identification of species arising from reactive adsorption of carbon oxides on metal oxide surfaces, Materials Chemistry, 7 (1982) 89-126. https://doi.org/10.1016/0390-6035(82)90059-1.
[88] M. Roiaz, E. Monachino, C. Dri, M. Greiner, A. Knop-Gericke, R. Schlögl, G. Comelli, E. Vesselli, Reverse Water–Gas Shift or Sabatier Methanation on Ni(110)? Stable Surface Species at Near-Ambient Pressure, Journal of the American Chemical Society, 138 (2016) 4146-4154. https://doi.org/10.1021/jacs.5b13366.
[89] F. Thibault-Starzyk, F. Maugé, Infrared Spectroscopy, Characterization of Solid Materials and Heterogeneous Catalysts, 1-48. https://doi.org/10.1002/9783527645329.ch1.
[90] S. Haq, J.G. Love, H.E. Sanders, D.A. King, Adsorption and decomposition of formic acid on Ni{110}, Surface Science, 325 (1995) 230-242. https://doi.org/10.1016/0039-6028(94)00694-6.
[91] K. Coenen, F. Gallucci, B. Mezari, E. Hensen, M. van Sint Annaland, An in-situ IR study on the adsorption of CO2 and H2O on hydrotalcites, Journal of CO2 Utilization, 24 (2018) 228-239. https://doi.org/10.1016/j.jcou.2018.01.008.
[92] G. Ramis, G. Busca, V. Lorenzelli, Low-temperature CO2 adsorption on metal oxides: spectroscopic characterization of some weakly adsorbed species, Materials Chemistry and Physics, 29 (1991) 425-435. https://doi.org/10.1016/0254-0584(91)90037-U.
[93] S.M. Lee, Y.H. Lee, D.H. Moon, J.Y. Ahn, D.D. Nguyen, S.W. Chang, S.S. Kim, Reaction Mechanism and Catalytic Impact of Ni/CeO2–x Catalyst for Low-Temperature CO2 Methanation, Industrial & Engineering Chemistry Research, 58 (2019) 8656-8662. https://doi.org/10.1021/acs.iecr.9b00983.
[94] Q. Liu, Y. Tian, One-pot synthesis of NiO/SBA-15 monolith catalyst with a three-dimensional framework for CO 2 methanation, International Journal of Hydrogen Energy, 42 (2017). https://doi.org/10.1016/j.ijhydene.2017.02.070.
[95] M.C. Bacariza, I. Graça, S.S. Bebiano, J.M. Lopes, C. Henriques, Micro- and mesoporous supports for CO2 methanation catalysts: A comparison between SBA-15, MCM-41 and USY zeolite, Chemical Engineering Science, 175 (2018) 72-83. https://doi.org/10.1016/j.ces.2017.09.027.
[96] H. Lu, X. Yang, G. Gao, J. Wang, C. Han, X. Liang, C. Li, Y. Li, W. Zhang, X. Chen, Metal (Fe, Co, Ce or La) doped nickel catalyst supported on ZrO2 modified mesoporous clays for CO and CO2 methanation, Fuel, 183 (2016) 335-344. https://doi.org/10.1016/j.fuel.2016.06.084.
[97] Y. Resing Dias, O. Perez-Lopez, Carbon dioxide methanation over Ni-Cu/SiO2 catalysts, Energy Conversion and Management, 203 (2020) 112214. https://doi.org/10.1016/j.enconman.2019.112214.
[98] S. Rahmani, M. Rezaei, F. Meshkani, Preparation of highly active nickel catalysts supported on mesoporous nanocrystalline γ-Al2O3 for CO2 methanation, Journal of Industrial and Engineering Chemistry, 20 (2014) 1346–1352. https://doi.org/10.1016/j.jiec.2013.07.017.
[99] H. Tao, S. Wang, R. Li, Y. Li, W. Yang, CO2 methanation over NiCe/Al2O3 catalysts: effect of nickel loading and particle size on catalytic performance, Ferroelectrics, 562 (2020) 10-16. https://doi.org/10.1080/00150193.2020.1760579.
[100] J. Kopula Kesavan, I. Luisetto, S. Tuti, C. Meneghini, G. Iucci, C. Battocchio, S. Mobilio, S. Casciardi, R. Sisto, Nickel supported on YSZ: The effect of Ni particle size on the catalytic activity for CO2 methanation, Journal of CO2 Utilization, 23 (2018) 200-211. https://doi.org/10.1016/j.jcou.2017.11.015.
[101] K. Hadjiivanov, Chapter Two - Identification and Characterization of Surface Hydroxyl Groups by Infrared Spectroscopy, Advances in Catalysis, 57 (2014) 99-318. https://doi.org/10.1016/B978-0-12-800127-1.00002-3.
[102] J. Zarfl, D. Ferri, T.J. Schildhauer, J. Wambach, A. Wokaun, DRIFTS study of a commercial Ni/γ-Al2O3 CO methanation catalyst, Applied Catalysis A: General, 495 (2015) 104-114. https://doi.org/10.1016/j.apcata.2015.02.005.
[103] P. Völs, S. Hilbert, B. Störr, N. Bette, A. Lißner, J. Seidel, F. Mertens, Methanation of CO2 and CO by (Ni,Mg,Al)-Hydrotalcite-Derived and Related Catalysts with Varied

Magnesium and Aluminum Oxide Contents, Industrial & Engineering Chemistry Research, 60 (2021) 5114-5123. https://doi.org/10.1021/acs.iecr.1c00028.
[104] K. Ito, H. Bernstein, The vibrational spectra of the formate, acetate, and oxalate ions, Canadian Journal of Chemistry, 34 (2011) 170-178. https://doi.org/10.1139/v56-021.
[105] J. Raskó, J. Kiss, Adsorption and surface reactions of acetaldehyde on alumina-supported noble metal catalysts, Catalysis Letters, 101 (2005) 71-77. https://doi.org/10.1007/s10562-004-3752-y.
[106] B. Miao, S.S.K. Ma, X. Wang, H. Su, S.H. Chan, Catalysis mechanisms of CO2 and CO methanation, Catalysis Science & Technology, 6 (2016) 4048-4058. https://doi.org/10.1039/C6CY00478D.
[107] H.L. Huynh, J. Zhu, G. Zhang, Y. Shen, W.M. Tucho, Y. Ding, Z. Yu, Promoting effect of Fe on supported Ni catalysts in CO2 methanation by in situ DRIFTS and DFT study, Journal of Catalysis, 392 (2020) 266-277. https://doi.org/10.1016/j.jcat.2020.10.018.
[108] S. Akamaru, T. Shimazaki, M. Kubo, T. Abe, Density functional theory analysis of methanation reaction of CO2 on Ru nanoparticle supported on TiO2 (101), Applied Catalysis A: General, 470 (2014) 405-411. https://doi.org/10.1016/j.apcata.2013.11.016.
[109] J.W. Han, J.S. Park, M.S. Choi, H. Lee, Uncoupling the size and support effects of Ni catalysts for dry reforming of methane, Applied Catalysis B: Environmental, 203 (2017) 625-632. https://doi.org/10.1016/j.apcatb.2016.10.069.